Available online at www.sciencedirect.com
SCIENCE DIRECT®
Coordination Chemistry Reviews 249 (2005) 1111–1132
COORDINATION CHEMISTRY REVIEWS
www.elsevier.com/locate/ccr

Review

Electronic structures and spectral properties of endohedral fullerenes

Suchi Guha[a,*], Kazuo Nakamoto[b]

[a] *Department of Physics and Astronomy, University of Missouri, Columbia, MO 65211, USA*
[b] *Department of Chemistry, Marquette University, P.O. Box 1881, Milwaukee, WI 53217, USA*

Received 29 September 2004; accepted 8 November 2004
Available online 5 January 2005

Contents

Abstract

Endohedral fullerenes belong to a new class of compounds which are technologically and scientifically important owing to their unique structures and optoelectronic properties. This review focuses on theoretical calculations and spectroscopic (electronic, vibrational, and nuclear magnetic resonance (NMR)) studies of endohedral fullerenes thus far published. A theoretical background, with various computational

* Corresponding author. Tel.: +1 573 8843687; fax: +1 573 8824195.
E-mail address: guhas@missouri.edu (S. Guha).

doi:10.1016/j.ccr.2004.11.017

methods used for determining energy-optimized electronic structure and calculation of vibrational spectra, is presented. Further, theoretical and spectroscopic investigations of individual endohedral fullerenes are discussed. Such studies provide structural information about the carbon cage, position of the encapsulated species, and the degree of charge transfer. In particular, ^{13}C NMR spectroscopy is indispensable for the determination of the cage symmetry. In some cases, NMR signals from ^{45}Sc encapsulated species yield information about dynamic behavior inside the cage. Vis–NIR absorption spectra determine the HOMO–LUMO band-gap energy. IR and Raman spectroscopy play an important role in elucidating the nature of interaction between the cage and encapsulated species. Novel vibrations resulting from these interactions appear in the low-frequency region, and the corresponding force constants serve as a measure of the strength of their interaction.

Keywords: Endohedral fullerenes; Density functional theory; UV–vis–NIR spectra; IR spectra; Raman spectra; C_{60}; C_{70}; C_{72}; C_{74}; C_{78}; C_{80}; C_{82}; C_{84}

1. Introduction

It was first proposed in 1985 that fullerenes could confine atoms in their interior because of their closed-cage structure [1]. Since then metal-containing endohedral fullerenes have attracted special attention as a new class of technologically relevant materials due to their combined fullerene-like and metallic properties. In most endohedral metallofullerenes, introduction of metal atoms into carbon cages leads to an increase in the electron affinity relative to the corresponding empty-cages [2,3]. Endohedral metallofullerenes hold great promise for applications in optoelectronic devices since varying the encapsulated metal cluster can alter the optical and electronic properties, without changing the structural features of the outer carbon shell. Enhancement of third-order nonlinear optical susceptibility observed in endohedral metallofullerenes further establishes them as potential candidates for nonlinear optical devices [4].

A variety of endohedral metallofullerenes have been reported, but their investigations have been severely limited because they are typically formed in extremely low yields (<0.5%). This article is intended to review the structural and spectroscopic investigations of the limited number of endohedral fullerenes thus far published [5–7] and for which UV–vis and vibrational data are available. These studies have shed light on the effect of encapsulation on the carbon cage, the location of the encapsulated species inside the cage, and the nature of interaction between the carbon cage and the encapsulated species. This review is organized as follows: Section 2 gives a theoretical background on electronic structure calculation of fullerenes and empirical models for Raman and infrared absorption intensity calculations. In Sections 3–8 we discuss the following fullerene cages: C_{60} and C_{70}, C_{72} and C_{74}, C_{78}, C_{80}, C_{82}, and C_{84}. In each of these sections, we first discuss the structure of empty fullerene cages followed by a discussion of their endohedral counterpart in terms of the electronic states, electronic and vibrational spectra, and nuclear magnetic resonance (NMR) spectra [5,7–9].

2. Theoretical background

Various theoretical techniques have been employed to study the electronic and structural (including vibrational) properties of fullerenes and their derivatives. These studies have revealed the structure of the fullerene cages, the electronic states of metal atoms and fullerene cages, and how the electronic properties and chemical reactivities of empty fullerene cages change upon endohedral metal doping. Recently, these investigations have been extended to endohedral fullerenes containing small molecules, such as Sc_3N and Y_2C_2. In this section we give a brief overview of some of the theoretical techniques of modern quantum chemistry that are used for the electronic and vibrational structure calculations of fullerenes and endohedral fullerenes.

2.1. A simple model for the electronic structure of C_{60}

For a perfectly spherical molecule, one can use spherical harmonics to predict the electronic energy levels. A model for the electronic structure of C_{60} based on elementary quantum mechanics and group theory can be found in Ref. [10]. The spherical nature of a C_{60} molecule allows the electronic states to be labeled by spherical harmonics [11]. In this simplest model the 60 π electrons of C_{60} are described by spherical harmonic wavefunctions modified slightly by the icosahedral symmetry. To accommodate 60 electrons according to the Pauli exclusion principle and Hund's rule, the energy states corresponding to $\ell = 0$ to $\ell = 4$ are completely filled. The highest energy level corresponding to $\ell = 5$ has 10 unpaired electrons. Since pristine C_{60} is an insulator and has no unpaired electrons, the above scheme needs to be modified. One has to invoke the icosahedral symmetry which is a lower symmetry compared to a perfect sphere. The carbon-derived potential splits the degenerate energy levels above $\ell = 2$ of the spherical potential. The $\ell = 5$ shell with 11 degenerate states splits into a five-fold degenerate highest occupied molecular orbital (HOMO), a threefold degenerate lowest unoccupied molecular orbital (LUMO) and an additional threefold degenerate level at a higher energy, as shown in Fig. 1. Fifty π electrons fill orbitals from $\ell = 0$ to 4 and 10 electrons occupy part of the $\ell = 5$ shell.

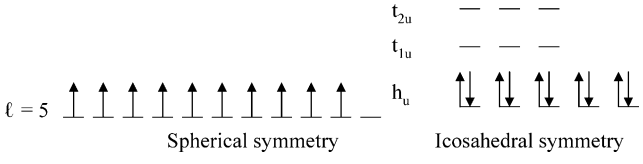

Fig. 1. The splitting of the $\ell = 5$ energy level under icosahedral symmetry. Adapted from Ref. [10].

The above model although quite simple correctly predicts the insulating behavior of C_{60} and the fact that the HOMO–LUMO transition ($h_u \rightarrow t_{1u}$) is optically forbidden. For an accurate description of the energy levels one must rely on more sophisticated molecular orbital or band theory calculations. A detailed theoretical approach for electronic structure calculations of fullerenes and their derivatives can be found in the work by Cioslowski [12].

2.2. Quantum chemical methods

Molecular quantum mechanical methods are classified as ab initio or semi-empirical. In semi-empirical methods a simpler Hamiltonian is used, compared to the actual molecular Hamiltonian, and typically uses parameters whose values are adjusted to fit experimental data. In contrast, an ab initio calculation uses the exact Hamiltonian. For a comprehensive review of the various ab initio and semi-empirical methods used in quantum chemistry, see Ref. [13].

Within non-relativistic quantum mechanics, the stationary wavefunctions of a chemical system composed of N electrons are the solutions of the time-independent Schrödinger equation. One normally invokes the Born–Oppenheimer approximation where the nuclei interact through an effective potential [14]. The total wavefunction $\Psi(\vec{r}_i, \vec{u}_i)$ can be approximately written as a product of the many-electron states, $\Psi_e(\vec{r}, \vec{u})$ and the nuclear wavefunction, $\Psi_N(\vec{u})$. The electronic states depend parametrically on the displacement of the nuclei, represented collectively by $\vec{u}$, and on the electronic coordinates $\vec{r}$. The electronic wavefunction can then be solved using

$$\hat{H}_e(\vec{r}, \vec{u})\Psi_e(\vec{r}, \vec{u}) = E_e\Psi_e(\vec{r}, \vec{u}), \tag{1}$$

where $\hat{H}_e = T_e + V_{ee} + V_{eN}$; T_e is the operator for the kinetic energy of electrons, V_{ee} is the potential energy of the repulsion between the electrons, V_{eN} is the potential energy of attraction between the electrons and the nuclei. Full specification of the electronic wavefunction, $\Psi_e(\vec{r}_1, \ldots, \vec{r}_N, \vec{u}_1, \ldots, \vec{u}_N)$ requires inclusion of the electronic spin.

For a system of N electrons there are $3N$ spatial and N spin coordinates. The spatial coordinates $\{\vec{r}_i\}$ are often combined with their spin to yield a set of $\{\vec{x}_i\}$. Ψ_e satisfies proper boundary conditions (vanishes at ∞) and the asymmetry property of the Pauli principle. In actual electronic structure calculations, it is often more convenient to work with the *one-particle reduced density matrix*:

$$\Gamma(\vec{x}_1', \vec{x}_1) = \sum_i n_i \psi_i^*(\vec{x}_1')\psi_i(\vec{x}_1), \tag{2}$$

which involves the one particle functions $\{\psi_i\}$ called *natural spinorbitals* [12]. The spinorbitals form an orthonormal set of functions and the corresponding occupation numbers $\{n_i\}$ sum up to N. The electron density $\rho(\vec{r})$ has maxima at the nuclear positions and decays exponentially at large distances. In the ab initio Hartree approximation the many electron wavefunction is written as a product of the single particle wavefunctions. Constraining the occupation numbers of the natural spinorbitals to either 0 or 1 leads to the Hartree–Fock (HF) approximation.

The choice of a basis set is an important starting point for most molecular quantum mechanical methods. For diatomic molecules, the basis functions are usually taken as atomic orbitals (AO). Each AO can be represented as a linear combination of one or more Slater-type orbitals (STO). For polyatomic molecules the above method is very time consuming; other methods, such as nuclei centered Cartesian Gaussian-type functions are used for large fullerene-type molecules [12]. The accuracy of computed wavefunctions improves with increasing number of basis functions. The basis sets fall into different categories such as, *minimal* (STO-3G, SZ), *split valence* (4-31G and 6-31G), *double-zeta* (DZ), *triple-zeta* (TZ), *polarized* (6-31G*, 6-311G*), and *diffuse* (6-311++G**). For a comprehensive review that explains the above terminology and which basis set should be used for a specific electronic calculation, see Ref. [15]. The above basis functions are available in the widely used ab initio program GAUSSIAN 03 [16].

The HF approximation ignores the correlation hole that each electron dresses itself with and hence overestimates the Coulomb repulsion between the electrons. Several approximate electron correlation methods have been proposed. Among these the Møller–Plesset second-order perturbation theory (MP2) is a feasible large-scale ab initio calculation of the ground state properties. Semi-empirical approaches of quantum chemistry have also played a vital role in the electronic structure calculations of organic molecules. See Chapter 2 of Ref. [12] for details on various ab initio and semi-empirical methods of electronic structure calculations and their application to fullerenes.

In recent years, density-functional theory (DFT), first propounded by Kohn and Sham [17], has become very popular in quantum chemistry for electronic structure calculations of larger molecules. The main difference between DFT and other ab initio methods is that in DFT one does not need the actual wavefunction; all that is required is the particle density, which explains all the observables. For a simple introduction to DFT, see Ref. [18]. The Hohenberg–Kohn theorem states that the electronic structure of a system of interacting electrons in the ground state in an external potential can be completely determined by the electronic charge density $\rho(\vec{r})$ [19]. The exact ground state energy functional can be written as:

$$E_G[\rho] = T[\rho] + \int \rho(\vec{r})V_N(\vec{r})\,d\vec{r} + \frac{1}{2}\int \rho(\vec{r})V_H(\vec{r})\,d\vec{r} + E_{XC}[\rho], \tag{3}$$

where $T[\rho]$ is the kinetic energy of interacting electrons, $V_N(\vec{r})$ is the electrostatic potential due to the nuclei, and

$V_H(\vec{r})$, the Hartree potential, is the electrostatic potential due to the electronic charge density $\rho(\vec{r})$. $E_{XC}[\rho]$ is the so-called exchange-correlation.

Many DFT calculations are performed in the local density approximation (LDA) [20,21], where the charge density is measured for a small volume element; E_{XC} assigned to this region is then approximated as the exchange-correlation energy of a volume element of a uniform electron gas of the same density as the initial volume element that was picked. This is an approximation since it ignores the fact that the charge density in the solid varies from one volume element to the next. In LDA, $E_{XC}(\rho)$ is given by an integral of a function, which is well known from quantum Monte Carlo calculations [22] and depends only on the local value of $\rho(\vec{r})$.

Bond dissociation energies obtained with the LDA method are much more accurate than those offered by Hartree–Fock calculations [23]. However, LDA is known to overestimate bond dissociation energies. This overbinding is reduced by the use of gradient-corrected functionals [24] in place of the local-density functionals. The gradient-corrected functionals depend not only on the electron density but also on its gradient [25]. The Becke functional [26], $E_x^B[\rho]$, for the exchange energy of a closed-shell system and the Lee–Yang–Parr (LYP) functional [27], $E_{corr}^{LYP}[\rho]$, for the correlation energy have been widely used. Although the exact correlation functional of the Kohn–Sham theory is different from describing the correlation energy in terms of the HF electron density, the same approximate functionals are often employed in both approaches. In the hybrid approach, the electron density is calculated with an ordinary self-consistent procedure, and the computed HF energy is combined with the approximate electron correlation energy. Accurate atomization energies, ionization potentials, and electron affinities are obtained within the hybrid approach, using the B3LYP functional, which depends on the one-particle density matrix rather than on the electron density itself, since it depends on the exact HF exchange energy $E_x^{HF}[\rho]$, and is given by

$$E_{corr}^{B3LYP}(\Gamma) = E_{corr}^{LYP}[\rho] + E_x^B[\rho] - E_x^{HF}[\rho]. \quad (4)$$

Electronic structure calculations based on DFT including electron correlation effects utilize only a fraction of computational time in comparison with wavefunction-based approaches of quantum chemistry. Both the Kohn–Sham and the hybrid formalisms have been implemented in a number of commercially available software packages, such as GAUSSIAN 03 [16] and Amsterdam density functional (ADF) [28], which are widely used for electronic structure calculations of fullerenes and endohedral fullerenes.

2.3. Ab initio calculations of endohedral fullerenes

The negative orbital energies of the occupied and virtual spinorbitals give the ionization potential (IP) and the electron affinities (EA), respectively, which is a direct consequence of Koopmans' theorem [29]. The philosophy behind this theorem is that the spinorbitals of the parent system do not change upon adding or removing an electron. One can also calculate the IPs and the EAs by separately carrying out HF calculations for the parent system and the corresponding ions. The differences between the respective IPs and the EAs yield the orbital relaxation energies. Table 1 gives the calculated IPs and the EAs (in eV) for M@C_{82} and pristine fullerenes, where M represents a metal atom [7]. The IP values for M@C_{82} are smaller, whereas the EA values of M@C_{82} are larger, than those for pristine C_{60} and C_{70}. This indicates that endohedral metallofullerenes can act as a strong electron donor as well as an electron acceptor.

Table 1
Calculated ionization potentials (IP) and electron affinities (EA) in eV for M@C_{82} and pristine fullerenes

	IP (eV)	EA (eV)
Sc@C_{82}	6.45	3.08
Y@C_{82}	6.22	3.20
La@C_{82}	6.19	3.22
Ce@C_{82}	6.46	3.19
Eu@C_{82}	6.49	3.22
Gd@C_{82}	6.25	3.20
C_{60}	7.78	2.57
C_{70}	7.64	2.69

Adapted from Ref. [7].

In endohedral metallofullerenes complexes, mixing between atomic orbitals of the guest and molecular orbitals of the fullerene host cage is negligible. Binding in these complexes is dominated by electrostatic and polarization effects [30]. However, in endohedral compounds such as charge-transfer complexes of C_{60}, C_{70} and other higher fullerenes, substantial orbital mixing may be present resulting in a direct chemical bonding [31]. See Ref. [12] for a detailed theoretical analysis on bonding and charge transfer in endohedral compounds and complexes.

Among various endohedral species, C_{28} is the smallest fullerene cage that successfully traps metal atoms inside the cage. HF-level calculations using a DZ basis set show that the binding energy of M@C_{28} (M: Mg, Al, etc.) is a good indicator of whether the C_{28} cage can trap metal atoms [32]. These calculations show that elements with electronegativities smaller than 1.54 eV are successfully trapped inside the C_{28} cage. Also, the smallest endohedral fullerene that can be formed for a given element is a function of its ionic radius. See Table III of Ref. [32] for further details.

To understand the motion of the encapsulated metals inside the fullerene cage, Nagase et al. [7] have investigated the electrostatic potential inside C_{80}, C_{82}, and C_{84} cages using HF calculations. Their finding is that the electrostatic potentials are all positive inside the cages, reflecting that the probability of finding electrons inside is much smaller than finding them outside. The situation changes drastically as electrons are transferred onto carbon cages. Electrostatic potentials calculated for C_{82}^{2-} and C_{84}^{4-} provide highly negative values implying that they are suitable for the accommodation of cationic species. The encapsulated metals, therefore, do not

preserve a neutral state but prefer a highly cationic state. The positively charged metal ions are highly stabilized at the minima of the electrostatic potentials. Hence, the electrostatic potentials play a dominant role in stabilizing endohedral metallofullerenes. In Sections 3–8, we will discuss the electronic structure of the various endohedral fullerenes in details.

2.4. Vibrational spectra

Several reviews have appeared on the vibrational structure of fullerenes and nanotubes [33,34]. An extensive review on the Raman and infrared spectroscopy of C_{60} by Menéndez and Page [35] gives a detailed description of the various normal mode calculations of C_{60} so far published. In the last decade there has been a rapid development in the first-principles calculations of the vibrational spectra of C_{60}, some of which are mentioned below.

First-principles normal mode calculations of fullerenes based on DFT within the LDA approach give the best agreement with the known C_{60} vibrational frequencies, with an average deviation ranging from 1.8% to 3.9%. The first principles approach of Quong et al. [36] and Wang et al. [37] using different all-electron localized basis sets within the LDA yield vibrational frequencies with deviations from the experimental values by 1.9% and 2.2%, respectively. Density functional perturbation theory was used by Giannozzi and Baroni [38] to compute the vibrational frequencies of C_{60}, with an average deviation from experiment of only 1.8%. The calculations by Adams et al. [39] uses the LDA and the Harris-energy-functional approximations [40], and expands the many-electron wavefunction as a sum of one 's' and three 'p' pseudoatomic local orbitals per atom. With subsequent refinement they obtained a deviation from experiment by 3.9%. A major advantage of their method is that it is computationally very efficient.

Since the early 1990s when experimental vibrational frequencies (Raman and IR) became available, several empirical methods were introduced and the force constants were calculated from fits to the Raman-active and infrared-active modes. Jishi et al. [41] used an eight-parameter model fit and Feldman et al. [42] used a seven-parameter model fit to the Raman-active and infrared-active modes. The adiabatic bond charge model, which is among the best empirical models for a description of the lattice dynamics of tetrahedral semiconductors and graphite, has also been applied to fullerenes [43].

In contrast to pristine fullerenes, there are only a few theoretical studies on the vibrational spectra of endohedral fullerenes. Inclusion of a metal cluster such as Sc_3N inside the fullerene cage may cause a significant amount of interaction between the cage and the metal cluster, and make such calculations more complex. The vibrational spectra are sufficiently sensitive to distinguish the various cage isomers. However, comparison with experiments is not quite satisfactory since the fullerene cage may have several isomeric forms which give similar frequencies.

2.4.1. Raman intensity calculations

A complete theoretical analysis of the Raman spectrum of fullerenes requires an accurate prediction of the Raman intensities. Both the Raman frequencies and intensities are sensitive to external perturbations such as, charge transfer, crystal field and the isotope effect [33]. Raman intensities of C_{60} have been calculated using ab initio methods [38], semi-empirical quantum chemical models [44], and empirical model, such as the bond polarizability model [45]. In this section we will limit our discussion to the prediction of Raman intensities using the bond polarizability model [46].

For a system of N atoms interacting via harmonic forces, the normal mode frequencies $\{\omega_f\}$ and amplitudes $\chi(f)$ of mode f, where $f = 1, \ldots, 3N$ labels the normal modes, are determined by a $3N \times 3N$ matrix eigenvalue equation:

$$(\mathbf{\Phi} - \omega_f^2 \mathbf{M})\chi(f) = 0, \tag{5}$$

where $\mathbf{\Phi}$ is the harmonic force constant matrix and $\mathbf{M}$ is the mass matrix. Both the force constant and mass matrices are symmetric. The mode eigenvectors $\boldsymbol{\chi}(f)$ are subjected to the orthonormality condition $\sum_{l\alpha} \chi_\alpha(l|f)\chi_\alpha(l|f')m_l = \delta_{ff'}$, where m_l is the mass of atom l and the sum is over all sites and directions. In the harmonic approximation, the intensity of off-resonance first-order Stokes scattering is given by

$$I_{\eta\eta'}(-\omega) = C\omega_L\omega_S^3 \sum_{f=1}^{3N} \frac{(\langle n(w_f)\rangle + 1)}{\omega_f} \left| \sum_{\alpha\beta} \eta'_\alpha \eta_\beta \boldsymbol{P}_{\alpha\beta,f} \right|^2 \times \delta(\omega - \omega_f), \tag{6}$$

ω_L and ω_S are the incident and scattered light frequencies; $\omega \equiv \omega_L - \omega_S$ is the Raman shift; η and η' are unit vectors along the incident and scattered polarization direction, respectively; $\langle n(\omega_f)\rangle \equiv [\exp(\beta\hbar\omega_f) - 1]^{-1}$ is the thermal average occupation number of mode f at temperature $T = (k_B\beta)^{-1}$. $\boldsymbol{P}_{\alpha\beta,f}$ is the derivative of the electronic polarizability tensor (where α and β are Cartesian coordinates) with respect to the normal coordinate of mode f.

The main assumption in the bond polarizability model is that the electronic polarizability of a molecule is equal to the sum of the electronic polarizabilities of the bonds between nearest pair of atoms. The overall polarizability $P_{\alpha\beta} = \sum_{j=1}^{N} \pi_{\alpha\beta}^j$ is expressed as the summation of the individual bond polarizabilities (π's) for the jth bond. One can show that the bond polarizability for a given pair of atoms can be written as the sum of an isotropic and an anisotropic tensor [47]

$$\pi_{\alpha\beta}(\vec{R}) = \frac{1}{3}(\alpha_{||} + 2\alpha_\perp)\delta_{\alpha\beta} + (\alpha_{||} - \alpha_\perp)\left(\frac{R_\alpha R_\beta}{R^2} - \frac{1}{3}\delta_{\alpha\beta}\right). \tag{7}$$

The principal assumption here is that bond polarizabilities are functions of the bond lengths "R" only, i.e. $\alpha_{||} = \alpha_{||}(R)$ and $\alpha_\perp = \alpha_\perp(R)$, where $\alpha_{||}$ is along the bond direction and $\alpha_\perp$ is along the principal axes perpendicular to the bond. This

approximation neglects the dependence of a bond's polarizability on the motion of atoms not connected to that bond. One can then show that

$$\boldsymbol{P}_{\alpha\beta,f} = -\sum_{B}\sum_{l\gamma}\left[\frac{\partial\pi_{\alpha\beta}[R(lB)]}{\partial R_{\gamma}(lB)}\right]_0 \chi_{\gamma}(l|f), \tag{8}$$

where the sum on B for a fixed site l runs over all bonds that are attached to the site. The above expression can be expressed as a sum of three contributions in terms of $\alpha_{||}$, $\alpha_{\perp}$ and their derivatives. See Ref. [47] for details. Using the mode eigenvectors obtained from first-principles calculations, together with the polarizability parameters, $\boldsymbol{P}_{\alpha\beta,f}$ can be calculated, which when substituted in Eq. (6) results in the first-order Raman intensity.

2.4.2. IR absorption intensity calculations

For a sample containing N molecules per unit volume, the first-order contribution to the absorption is given by [35]

$$A(\omega) = \frac{2\pi^2 N}{3cn}\sum_{f}|\vec{\mu}_f|^2\delta(\omega-\omega_f), \tag{9}$$

where n is the medium's refractive index, c is the speed of light in vacuum, and $\vec{\mu}_f$ is the derivative of the dipole moment. Therefore, the integrated absorption strength of a mode f is proportional to $|\vec{\mu}_f|^2$, which is related to the mode's effective charge.

In the literature there are several first-principles models that compute the IR strengths in C_{60} and C_{70}. Table 6 of Ref. [35] gives the calculated relative absorption strengths of the first-order IR active modes in C_{60}, using semi-empirical and first-principles (LDA) models. These theoretical IR strengths show a wide variation from model to model. Theoretical prediction of first-order IR strengths in C_{60} is more challenging since they depend quite sensitively on the electronic states; derivatives of the mode dipole moment ($\vec{\mu}_f$) describe the vibrationally induced electronic charge redistribution and are more difficult to predict. It turns out that several phenomenological models, such as the classical model for effective charges developed by Fabian [48] predict the IR strengths in C_{60} quite accurately. This model depends only on the geometry of the vibrating molecule where the dipole moment of a give mode is described by the motion of 60 π electrons. For a review of the several first-principles and phenomenological models that have been used for computing the IR strengths in pristine fullerenes, see Ref. [35].

3. C_{60} and C_{70}

The C_{60} cage consists of 20 hexagonal and 12 pentagonal faces with 60 carbon atoms being located at the vertices of a regular truncated icosahedron of I_h symmetry. A C_{60} molecule follows the isolated pentagon rule (IPR), which states that fullerenes with adjacent pentagons have a higher formation energy than fullerenes with isolated pentagons, whereby a pentagon is completely surrounded by hexagons. Since all the carbon atoms in C_{60} are equivalent, its ^{13}C NMR spectrum exhibits a single signal at 143.23 ppm. The 174 ($3\times60-6$) normal vibrations of the C_{60} cage are classified into $2A_g + A_u + 3F_{1g} + 4F_{1u} + 4F_{2g} + 5F_{2u} + 6G_g + 6G_u + 8H_g + 7H_u$ under I_h symmetry [49]. However, only four F_{1u} vibrations are IR-active and two A_g and eight H_g vibrations are Raman-active due to its high symmetry. As a result, four IR bands are observed at 527 cm^{-1} ($F_{1u}(1)$), 577 cm^{-1} ($F_{1u}(2)$), 1183 cm^{-1} ($F_{1u}(3)$) and 1428 cm^{-1} ($F_{1u}(4)$), and ten Raman bands are observed at 273 cm^{-1} ($H_g(1)$), 437 cm^{-1} ($H_g(2)$), 496 cm^{-1} ($A_g(1)$), 710 cm^{-1} ($H_g(3)$), 774 cm^{-1} ($H_g(4)$), 1099 cm^{-1} ($H_g(5)$), 1250 cm^{-1} ($H_g(6)$), 1428 cm^{-1} ($H_g(7)$), 1470 cm^{-1} ($A_g(2)$) and 1575 cm^{-1} ($H_g(8)$) [50]. In general, vibrations above 1000 cm^{-1} are predominantly due to displacements tangential to the C_{60} cage surface, whereas those below 800 cm^{-1} are predominantly due to radial displacements. The two polarized (A_g) Raman bands at 496 and 1470 cm^{-1} are assigned to the totally symmetric radial "breathing" and "tangential stretching" (or pentagonal pinching) modes, respectively, while the lowest frequency band (depolarized) at 273 cm^{-1} is described as the "cage-squashing" mode (vide infra).

A standard technique in molecular spectroscopy is the investigation of isotope-induced shifts in the frequencies of vibrational modes. Since the natural abundance of ^{13}C is 1.11%, 49% of all C_{60} molecules made from natural graphite contain one or more ^{13}C isotopes. High resolution Raman spectra of C_{60} molecules show that the pentagonal pinch mode at 1470 cm^{-1} has a fine structure due to the isotopic shifts. Fig. 2 shows a high-resolution Raman spectrum of the 1470 cm^{-1}

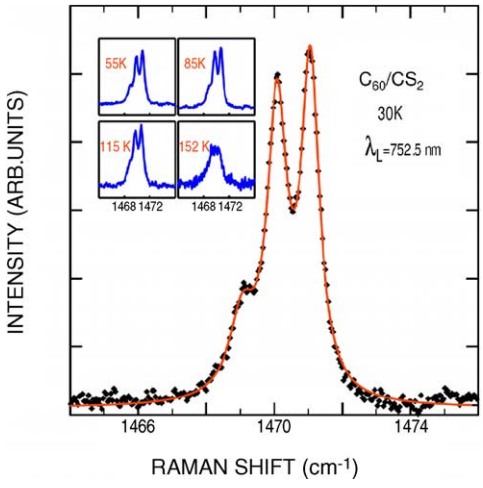

Fig. 2. Unpolarized Raman spectrum of a frozen solution of C_{60} in CS_2 at 30 K. The solid line is a 3-Lorentzian fit to the experimental data. The highest frequency is assigned to the totally symmetric pentagonal-pinch A_g mode in $^{12}C_{60}$. The other two lines are assigned to the pentagonal-pinch mode in molecules containing one and two ^{13}C isotopes, respectively. The inset shows the evolution of these peaks as the solution is heated. Reproduced from Ref. [51] with permission.

mode [51]. Three peaks are resolved, which show a striking correlation with the mass spectrum of C_{60} [52]. The highest energy Raman peak at 1471 cm^{-1} is the A_g mode of isotopically pure C_{60} (60 ^{12}C atoms). The second peak at 1470 cm^{-1} is from C_{60} molecules with one ^{13}C isotope, and the third peak at 1469 cm^{-1} is assigned to C_{60} molecules with two ^{13}C isotopes.

The C_{70} molecule can be described as two hemispherical caps of C_{60} molecules joined together by a belt of 10 carbon atoms [53]. There are eight different bond lengths in C_{70} ranging from 1.40 to 1.45 Å. It has a point group symmetry of D_{5h}. The lower symmetry of C_{70} in comparison to C_{60} results in many more Raman-active and infrared-active modes. Group theoretical analysis indicates that C_{70} has 53 Raman-active modes and 31 infrared-active modes. The Raman-active modes correspond to the symmetry types $12A_1' + 19E_1'' + 22E_2'$ and the infrared-active modes to $10A_2'' + 21E_1'$.

The Raman scattering intensities in molecular C_{60} and C_{70} are found to be well reproduced by a bond polarizability model with parameters similar to those obtained from hydrocarbons. The hydrocarbon polarizability parameters give a qualitative agreement with the experimental Raman spectra of C_{60} and C_{70}. A marked improvement for C_{60} was found for a bond polarizability fit to the experimental Raman spectra obtained using off-resonance near infrared excitation [54]. Fig. 3 (thin solid line) shows the Raman intensities of C_{60} obtained using first-principles vibrational eigenvectors along with the fit polarizability parameters [47] within the bond polarizability model. Recent work by Ren et al. [55] have further improved the set of polarizability parameters for C_{60}. It has been further shown that the polarizability parameters obtained for C_{60} can be transferred to higher fullerenes, such as C_{70} and C_{60} polymers [56] to predict the Raman spectra. The important consequence of this is that since the polarizabilities are independent of the chemical environment they are transferable between different compounds. As a result one can predict the Raman intensities of new fullerene systems. So far, to our knowledge there has been no published work on extending the bond polarizability model for predicting Raman intensities in charge-transfer or endohedral fullerene cages.

The degree of electronic coupling to the π electron system of the fullerene depends on the nature of the endohedral atoms. The charge transfer process in metallic endohedral fullerenes is more complex than in exohedral alkali metal-doped fullerenes. In the next section we first discuss the electronic states of exohedral metal-doped C_{60} followed by the electronic structures of endohedral C_{60} and C_{70}.

3.1. Electronic states of alkali-doped exohedral C_{60}

The interest in electronic properties of fullerenes dramatically increased after the discovery of superconductivity at 18 K in potassium doped C_{60} [57]. By intercalating C_{60} with alkali metals, a variety of new compounds have been formed. There are three distinct bulk phases: (a) the superconducting

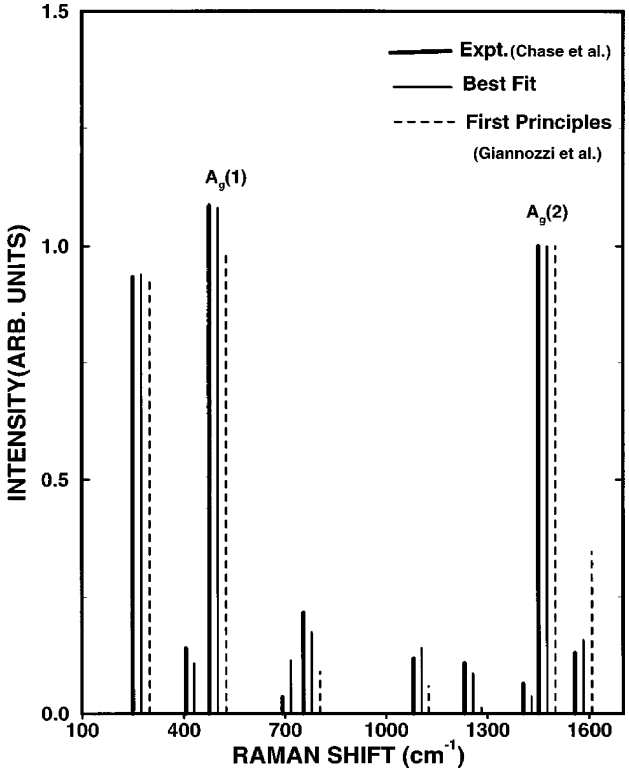

Fig. 3. Experimental and predicted normalized Raman spectra of C_{60}. The intensity of the $A_g(2)$ line at 1470 cm^{-1} has been set equal to unity, and the calculated lines have been shifted from the experimental frequency, for clarity. The thick solid line represent the experimental data of Chase et al. [54], and the thin solid lines show the fit obtained from fitted polarizability parameters. Reproduced from Ref. [47] with permission.

M_3C_{60}, where M refers to an alkali metal; (b) the insulating M_6C_{60} phase which adopts a body-centered structure (bcc); and (c) an intermediate composition M_4C_{60} of orthorhombic structure which is also insulating [58]. Spectroscopic studies on these compounds provide information about the perturbation of the C_{60} structure resulting from metal to C_{60} cage charge-transfer and the strength of the metal–C_{60} cage interaction. A wide variety of experimental techniques like optical absorption, [59] electron energy-loss spectroscopy [60] and nuclear magnetic resonance [61] have been used to probe the electronic states of the fullerenes.

The bonding character of an isolated C_{60} molecule is predominantly sp^2 with a small admixture of sp^3 character due to nonzero curvature. The electronic states can be decomposed into "π"-like and "σ"-like states. The curvature of the surface at a carbon atom induces a change in hybridization as compared to graphite. As a result the π-like orbital is no longer purely p_z orbital in character and the σ-like orbital contains an admixture of p_z. Thus the fullerenes are of intermediate hybridization.

Fig. 4 shows a schematic of the near-gap energy levels of an isolated C_{60}, and anions of the molecule, C_{60}^{3-} and C_{60}^{6-}, predicted by theoretical models [62,63]. It also shows the number of electrons in each level. The HOMO level is the h_u state and is fully occupied by 10 electrons.

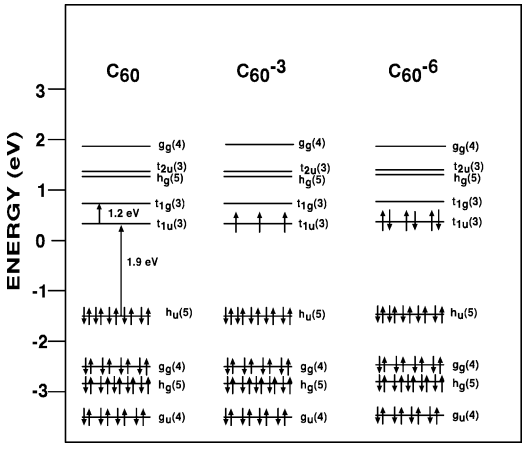

Fig. 4. Schematic near gap energy levels of C_{60}, C_{60}^{3-} and C_{60}^{6-}. The arrows in each level indicate electronic spins and the numbers in parenthesis denote the degeneracy of each level.

The HOMO–LUMO energy gap (between the h_u state and the t_{1u} state) is 1.9 eV. The lowest optically allowed transition between the valence band and the conduction band is from the h_u state to the $t_{1u} + 1$ (t_{1g}) state in a C_{60} molecule. For the C_{60} anions the picture is slightly different. In C_{60}^{3-} the LUMO is half filled i.e., it has three electrons and the transition between this state and the next higher state, the t_{1g} state, is optically allowed. As a result C_{60}^{3-} is a conductor, as opposed to C_{60}, which is an insulator. This is observed in the M_3C_{60} compounds, whereby a C_{60} molecule is ionized to C_{60}^{3-}. In fact these compounds exhibit superconductivity between 18 and 30 K. In C_{60}^{6-}, the LUMO is fully occupied with six electrons and hence this material is insulating.

Metallic conductivity has been observed for C_{60} when doped within a very narrow stoichiometry range. It turns out that metallic endohedral C_{60} is difficult to produce. This failure is attributed to the hybridization of metal 'd' orbitals with the carbon orbitals resulting in a donor–acceptor type bonding [64].

3.2. Endohedral C_{60} and C_{70}

A characteristic feature of endohedral fullerenes such as N@C_{60}, P@C_{60}, and N@C_{70} is that the enclosed atoms keep their ground state configurations and are localized in the center of the fullerenes. The atoms are freely suspended in the fullerene cages and exhibit properties resembling those of ions in electromagnetic traps [65]. A special feature of N@C_{60} is that it gives a clear hyperfine split electron paramagnetic resonance (EPR) signal even in the solid state [66]. This makes it an ideal probe for monitoring chemical reactions of C_{60} via changes in the EPR signal. Multiple functionalization of the cages of N@C_{60} and N@C_{70} are possible without destroying the endohedral system. A second possible use of N@C_{60} is in quantum computing [65] mainly due to the long spin lifetimes and the fact the system can be controlled at ambient conditions.

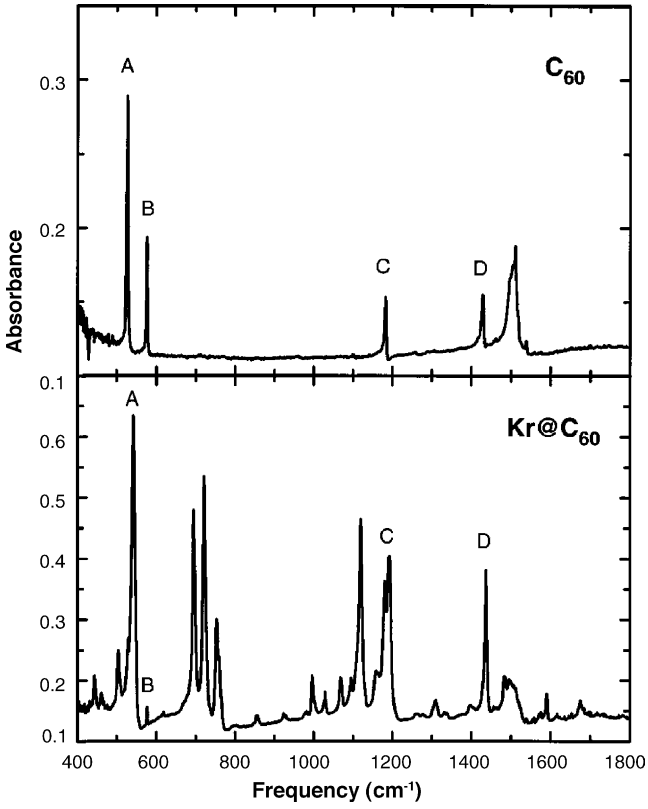

Fig. 5. The infrared spectra of C_{60} (top panel) and Kr@C_{60} (bottom panel). Adapted from Ref. [67].

Isolation of M@C_{60} (M: alkaline earth and lanthanide metal) has been limited due to difficulties in purification and the instability of the endohedral complexes. Other endohedral C_{60} and C_{70} systems, such as Kr@C_{60} [67] and Dy@C_{60} [68] have been isolated. In these structures the π-orbital system is perturbed. In particular, the Raman spectrum of Dy@C_{60} shows that three electrons are transferred from the Dy atom to the C_{60} cage, which is very different from N@C_{60} discussed previously. In the following sections we first consider two examples, Kr@C_{60} that has been successfully isolated, and LiC_{60} that exists as interstitial, exohedral Li and C_{60} and Li@C_{60} [69]. This is followed by a few examples of C_{60} encapsulating rare-earth metal atoms.

3.2.1. Kr@C_{60}

Yamamoto et al. [67] isolated 140 μg of 90% pure Kr@C_{60} from a mixture containing 99.9% empty C_{60} and measured its ^{13}C NMR, IR and UV–vis spectra. The ^{13}C NMR spectrum of a mixture of 40% C_{60} and 60% Kr@C_{60} exhibits two signals at 143.23 and 143.62 ppm, respectively. Thus, encapsulation of a Kr atom in the C_{60} cage causes no perturbation of the I_h symmetry on the NMR time scale although a downfield shift of 0.39 ppm is observed.

Fig. 5 compares the IR spectra of C_{60} and Kr@C_{60}. In the former, the four IR-active (F_{1u}) bands mentioned previously are marked by A, B, C and D. The extra band at 1500 cm^{-1} is due to the solvent CS_2, which remained in the sample film

after solvent evaporation. Bands A, C and D of $Kr@C_{60}$ are readily identifiable. The shoulder bands on the low-frequency side are due to empty C_{60} (10%). Band B is unexpectedly weak although the reason for it is not clear. Other bands were attributed to unidentifiable impurities. It was noted that Bands A, C and D were shifted to higher frequencies by 15.4, 10.6 and 8.2 cm^{-1}, respectively, upon encapsulation of a Kr atom. In addition to the normal modes of the carbon cage, $Kr@C_{60}$ is expected to show three IR-active (F_{1u}) vibrations corresponding to three degrees of freedom of the encapsulated Kr atom. However, their frequencies are estimated to be near 100 cm^{-1} which was far below the measurable range.

Fig. 6 compares the UV–vis spectra [67] of C_{60} and $Kr@C_{60}$. In the 640–580 nm region, all four bands, γ_0, γ_1, γ_2 and γ_3 are red-shifted upon encapsulation of the Kr atom. These bands have been assigned to the components of a symmetry-forbidden $^1T_{1g} \leftarrow {}^1A_{1g}$ transition. Note that the A_{1g} level lies deep down in the valence band, not shown in Fig. 4. γ_0 and γ_2 are the false origins separated from γ_1 and γ_3, respectively, by one quantum of the lowest H_g vibration which was estimated to be 254 or 257 cm^{-1} for $Kr@C_{60}$. Thus, incorporation of a Kr atom does not change or slightly increases the vibrational frequency of this H_g mode. The bands in the 420–370 nm region have been assigned to the allowed $1\ ^1T_{1u} \leftarrow {}^1A_{1g}$ transition with A_0 as the origin, and encapsulation of a Kr atom slightly increased its frequency by 10–15 cm^{-1}. This change is smaller and in the opposite direction compared to the former symmetry-forbidden system. The separations of A_1, A_2 and A_3 from the origin were previously assigned to single quanta of the lowest frequency $H_g(1)$, $A_g(1)$ and $H_g(5)$ modes, respectively, in the 1^1T_{1u} state. Thus, Yamamoto et al. [67] determined these frequencies to be 249, 429 and 1040 cm^{-1}, respectively. Thus encapsulation reduces these frequencies by ~1% in the 1^1T_{1u} electronic state. All the above results suggest that incorporation of the Kr atom into the C_{60} cage does not lower the symmetry although it slightly perturbs the π-orbital system. This result is expected since no charge-transfer occurs from the Kr atom to the cage.

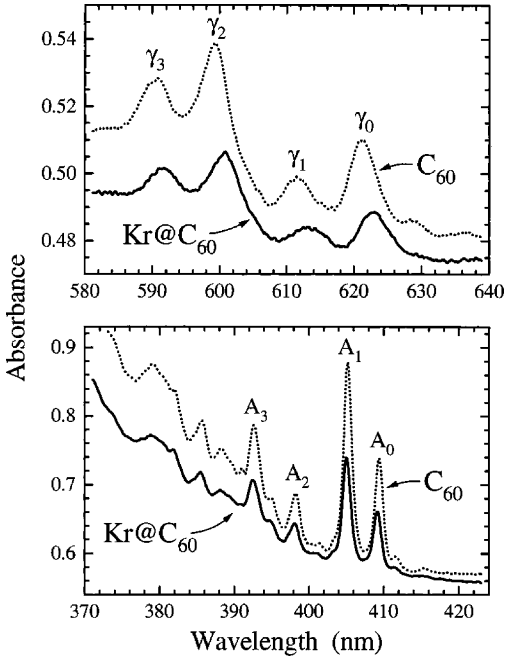

Fig. 6. Ground-state absorbance spectra of $Kr@C_{60}$ and C_{60} dissolved in methylcyclohexane/isopentane glasses at 77 K. Adapted from Ref. [67].

3.2.2. *Li@C60*

Jantoljak et al. [69] carried out a vibrational study on lithium-implanted fullerene films (LiC_{60}), which include 25% endohedral $Li@C_{60}$ as well as interstitial, exohedral Li and C_{60} matrix. Fig. 7 compares the Raman spectra of LiC_{60} and pristine C_{60}. In general, the bands observed for

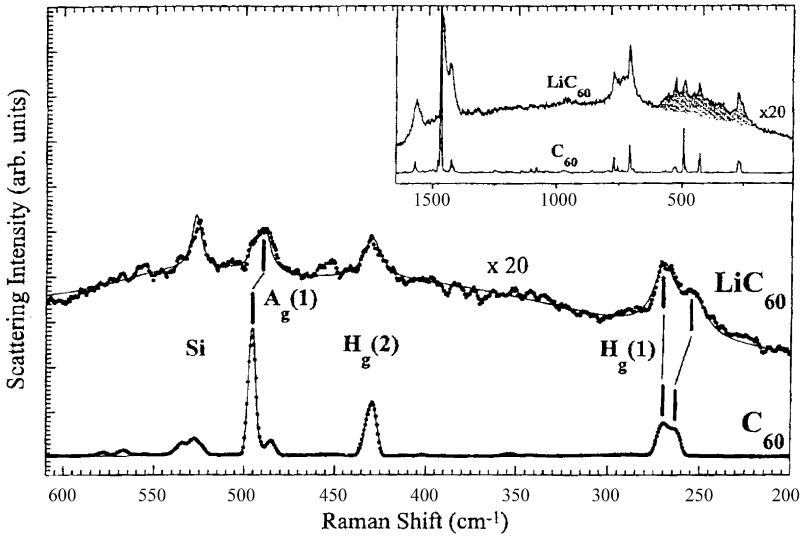

Fig. 7. Comparison of the Raman spectrum of a pure and a lithium-implanted C_{60} film at 20 K with the 514.5 nm line as the excitation line. The inset shows additional vibrational–rotational band from the two compounds. Reproduced from Ref. [69] with permission.

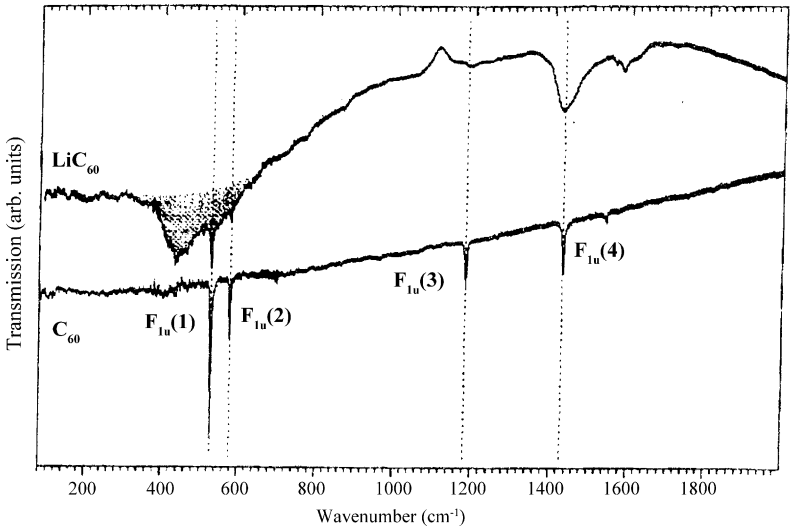

Fig. 8. Infrared absorption spectrum of LiC_{60} and C_{60}. Additional absorption is seen in LiC_{60} between 350 and 600 cm^{-1} region. Reproduced from Ref. [69] with permission.

LiC_{60} are broadened and some are shifted to lower frequencies relative to those of C_{60}. The pentagonal pinching ($A_g(2)$) frequency near 1470 cm^{-1} is known to be shifted by ~7 cm^{-1} to a lower frequency per one electron transfer. In the present case, this band shifts from 1468.5 to 1464.2 cm^{-1}, indicating one electron transfer on average in every second C_{60} cage. The background in the 600–250 cm^{-1} region (shaded area of the inset) was attributed to the vibrational–rotational transitions predicted theoretically. The same background is also observed in the IR spectrum shown in Fig. 8. It is seen that the intensities of the $F_{1u}(1)$ and $F_{1u}(2)$ modes are reduced approximately by a factor of 1/3, although their frequencies and widths are almost unchanged. This is contrast to intercalated fullerenes such as $(K,Rb)_xC_{60}$ in the metallic state where the $F_{1u}(2)$ mode becomes much stronger than the $F_{1u}(1)$ mode and the latter is shifted significantly to a lower frequency as x increases. Furthermore, the $F_{1u}(3)$ mode disappears and the $F_{1u}(4)$ mode is broadened considerably without changes in frequency. These differences in IR spectra between LiC_{60} and $(K,Rb)_xC_{60}$ support the interpretation that the former contains endohedral $Li@C_{60}$. It was not possible, however, to separate the contributions of the interstitial and exohedral species from that of the endohedral fullerene in these spectra.

3.2.3. M@C_{60} (M: rare-earth metal)

Isolation of $M@C_{60}$, where M refers to a rare-earth metal atom, has been difficult since it is unstable in air and soluble in solvents that are not suitable for high-performance liquid chromatographic (HPLC). $Er@C_{60}$ was first purified by Ogawa et al. [70] via a combined technique of vacuum sublimation followed by HPLC separation. A UV–vis and near-IR absorption spectrum of $Er@C_{60}$ in aniline shows a characteristic peak at 500 nm with an onset at 1200 nm, which is far in the red compared to that of C_{60} in aniline. Since the metallofullerenes are better electron acceptors than the empty fullerenes, $Er@C_{60}$ may be slightly stabilized by forming a weak charge-transfer complex with aniline.

Inoue et al. [71] isolated $Eu@C_{60}$ and observed the onset of the absorption red shifted (>900 nm) in comparison with those of C_{60} and C_{70}. The valence state of the Eu atom was determined to be 2+ by Eu L_{III}-edge X-ray absorption near-edge spectroscopy (XANES). Basically XANES is a type of X-ray absorption fine-structure spectroscopy (XAFS) which uses the technique of modulating the X-ray absorption coefficients at energies near and above an X-ray absorption edge. Typically XANES is a region of the X-ray absorption spectrum within ~50 eV of the absorption edge. The oscillatory structure in the X-ray absorption coefficient turns out to be a unique signature of a given material yielding information on the local atomic coordination, chemical/oxidation states with minimum sample requirements. For a review on the XAFS/XANES see Ref. [72].

The first report of an endohedral C_{60} with metallic properties was on $La@C_{60}$. Klingeler et al. [73] deposited individual clusters of $La@C_{60}$ onto graphite and used scanning tunneling spectroscopy (STS) to probe the local density of states. STS determines the local electronic structure of a sample's surface and encompasses various methods. One of the methods is to use a scanning tunneling microscope in order to collect current versus voltage (I–V) curves at every point in a data set, providing a three-dimensional map of the electronic structure. With a lock-in amplifier, dI/dV (conductivity) versus voltage curves can be collected directly. Fig. 9 shows the normalized differential tunneling conductivity as a function of the bias voltage for $La@C_{60}$. A metal-like density of states (zero band-gap) at the Fermi level (zero voltage) in $La@C_{60}$ is revealed. This can be interpreted in terms of charge donation from the La atom to the C_{60} derived π orbitals. The C_{60}-derived LUMO is expected to split in $La@C_{60}$ due to charge transfer and symmetry reduction. $La@C_{60}$ becomes metallic since t_{1u}-derived orbital is partially filled upon charge

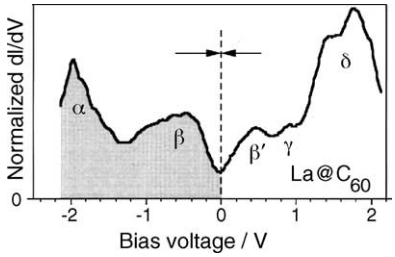

Fig. 9. The normalized differential tunneling conductivity (d*I*/d*V*)(*V*/*I*) as a function of the negative and positive bias voltages of La@C_{60} on graphite at room temperature. Adapted from Ref. [73].

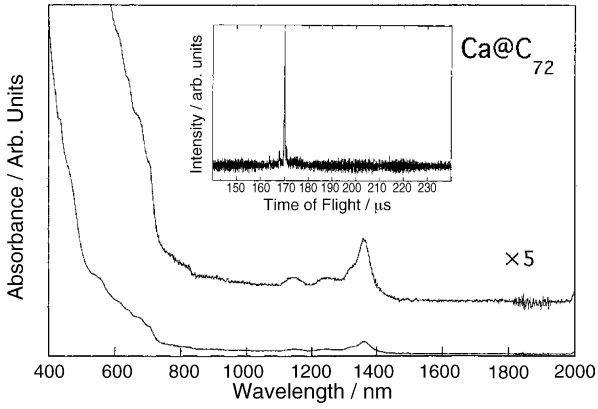

Fig. 10. UV–vis–NIR absorption spectrum of isolated Ca@C_{72} in CS_2 solution. The insert shows a LD–TOF mass spectrum of the isolated Ca@C_{72}. Reproduced from Ref. [77] with permission.

transfer. Moreover, the tunneling current of La@C_{60} at room temperature increases linearly with the bias voltage, which changes at lower temperatures; the cluster shows a reversible opening of a band-gap at a transition temperature of ∼28 K.

The metal-like density of states in La@C_{60} results due to a charge donation from the trivalent La atom into C_{60} derived π orbitals ($La^{3+}@C_{60}^{3-}$), as shown in Fig. 4. Owing to the non-centrosymmetrical position of the La atom inside the C_{60} cage and charge donation, the icosahedral symmetry of C_{60} is lowered. This results in splitting of the C_{60}-derived LUMO level and the t_{1u} level is only partially filled as shown in Fig. 9. Consequently, the peaks below (β) and above (β′) the Fermi energy can be assigned to the t_{1u}-derived orbitals. The Fermi level is located within this split-orbital unlike C_{60}, where the Fermi level lies between the h_u and the t_{1u} levels. The metallic properties of La@C_{60} opens up the possibility of superconductivity and ferromagnetism of endohedral fullerenes doped with rare-earth atoms.

Endohedral fullerenes of carbon cage size in the range between C_{66} and C_{84} are shown to be stable structures although the corresponding empty fullerenes are either not stable or have been isolated only in minor quantities in the fullerene soot. Amongst these, many of them do not follow the IPR rule. There are several ways in which the IPR can be violated; one way is to generate fused-pentagons in which the pentagons are adjacent to one another. Isolation and structure determination of $Sc_2@C_{66}$ [74] and $Sc_3N@C_{68}$ [75] from NMR spectra clearly show that these carbon cages have non-IPR structures. The $Sc_2@C_{66}$ X-ray structure is of space group *Pmn*2 and the structure contains two pairs of two-fold fused pentagons with closely situated two Sc atoms [74]. The yield and stability of fullerenes with carbon cages in the size group C_{70} and C_{84} strongly depend upon the enclosed metal. Dunsch et al. [76] have isolated various metallofullerenes such as $La_2@C_{72}$, $Ce_2@C_{72}$, Eu@C_{74}, Tm@C_{78}, and $Sc_3N@C_{80}$. $La_2@C_{72}$ and $Ce_2@C_{72}$ show similar features in their absorption. The stability of Tm@C_{78} is much lower than Eu@C_{74}. In the following sections we discuss only a limited number of endohedral fullerenes and mainly focus on those where the UV–vis and vibrational spectra have been measured.

4. C_{72} and C_{74}

4.1. *Ca@C_{72} and Ca@C_{74}*

Thus far, empty C_{72} and C_{74} cages have not been isolated even in microscopic quantities although their IPR structures are expected to be of D_{6d} and D_{3h} symmetries, respectively. However, Wan et al. [77] were able to obtain samples of pure Ca@C_{72} and Ca@C_{74} enough to measure their UV–vis spectra in CS_2 solution. As shown in Fig. 10, Ca@C_{72} exhibits the spectrum with the onset of absorption near 1500 nm followed by several peaks in the 1200–1400 nm region. Such low energy peaks in the absorption spectrum cannot be attributed to energy gaps between the valence band (HOMO) and the conduction band (LUMO). The origin of these transitions is most probably from the LUMO to LUMO + *n*th level. These features are characteristic of the metal → cage electron-transfer. Successful isolation of these endohedral fullerenes suggests that an unstable carbon cage can be stabilized by metal to cage charge-transfer. Fig. 11 illustrates two geometry-optimized structures of Ca@C_{74} based on ab initio calculations obtained by these workers. In their method the geometry optimization was done at the HF level with a 3-21G basis set for the carbon atoms (see Section 2.2). In Fig. 11, (a) is more stable than (b), and the Ca atom is along the symmetry axis but not at the center of symmetry. As a result, the overall symmetry is reduced from D_{3h} to C_{2v}. Ab initio calculations by Kobayashi

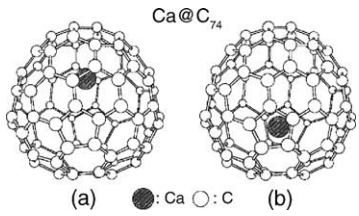

Fig. 11. Optimized structures of Ca@C_{74} ab initio calculation. Structure (a) is 7 kcal/mol more stable than structure (b). Since the calcium atom is not in the center, the symmetry of both structures decreases from D_{3h} to C_{2v}. Reproduced from Ref. [77] with permission.

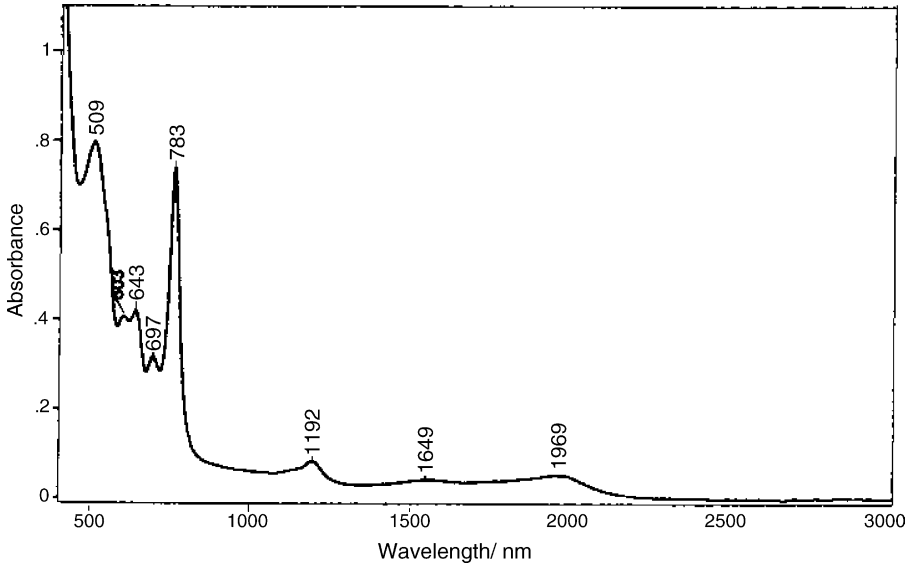

Fig. 12. vis–NIR spectrum of Eu@C_{74} in CS_2 solution. Reproduced from Ref. [80] with permission.

and Nagase [78] and Akasaka and coworkers [79] have been carried out using Gaussian 94 (previous version of Gaussian 03 [16]) at the Hartree–Fock level with subsequent improvements using the BLYP energy levels and the 6-31G basis set (see Section 2.2). These calculations suggest that more stable structures may be obtained if one considers non-IPR structures. For example, they suggested one structure containing a pair of adjacent pentagons and another structure containing one heptagon surrounded by five adjacent pentagons. These predictions were partly confirmed by later experimental work [74,75].

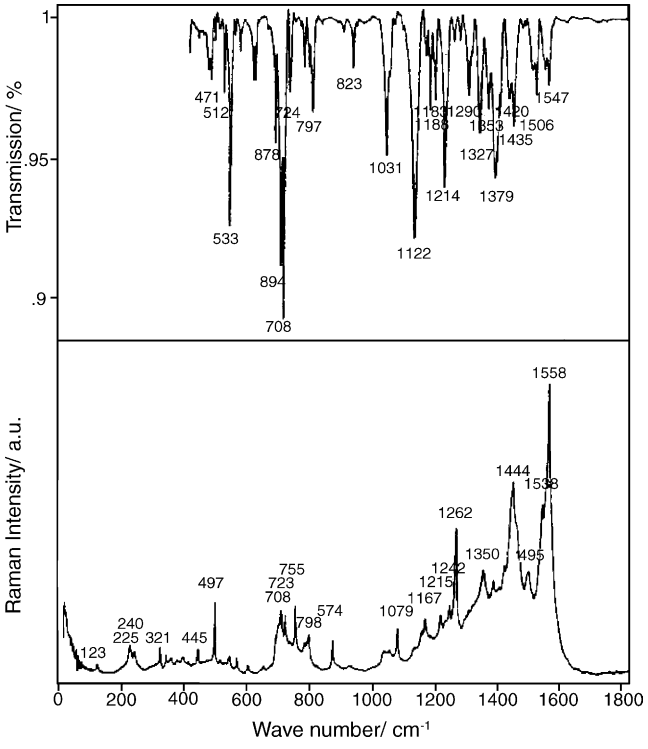

Fig. 13. IR and Raman spectrum of solid Eu@C_{74}. Reproduced from Ref. [80] with permission.

4.2. *Eu@C_{74}*

Kuran et al. [80] isolated the first europium endohedral fullerene, Eu@C_{74}, and measured its vis–NIR, IR, Raman and ESR spectra. As seen in Fig. 12, it exhibits eight absorption maxima in the 500–2500 nm region (CS_2 solution). All these bands were assigned to the $\pi \rightarrow \pi^*$ transitions of the carbon cage because they blue-shift upon changing the solvent to toluene which is less polar. Fig. 13 shows the IR and Raman spectra obtained in the solid state. Both spectra exhibit approximately 50 bands in the 1600–200 cm^{-1} region where the carbon cage vibrations appear. These numbers are more than those expected from the strict selection rules of D_{3h} point group. Thus, the symmetry of Eu@C_{74} must be lower than D_{3h}. The Raman band at 123 cm^{-1} was assigned to the Eu–C_{74} cage vibration based on vibrational frequencies known for other endohedral metallofullerenes.

5. C_{78}

The C_{78} cage consists of 12 pentagons and 29 hexagons which lead to five IPR structures of D_3, C_{2v}(a), C_{2v}(b), D_{3h}(a), and D_{3h}(b). Thus far, three stable isomers have been isolated, and their symmetries (C_{2v}(a), C_{2v}(b), D_{3h}) have been confirmed by ^{13}C NMR spectroscopy [81]. $Sc_3N@C_{78}$ is more abundant than any of the other conventional metallofullerenes such as $Sc_2@C_{84}$. Olmstead et al. [82] have isolated $Sc_3N@C_{78}$, characterized it by UV–vis spectroscopy, and carried out X-ray analysis on $[Sc_3N@C_{78}]Co(OEP)1.5C_6H_6 0.3CHCl_3$(OEP: oc-

taethylporphyrin). The UV–vis absorption spectrum of air-stable $Sc_3N@C_{78}$ in CS_2 shows peaks at 460, 623 nm with shoulders at longer wavelengths. These workers proposed an overall D_{3h} symmetry. Recently Campanera et al. [83] have carried out DFT calculation of $Sc_3N@C_{78}$ (theoretical mechanism is described in Section 6.2). They find that the metal ions are strongly linked to three [6:6] junctions of three different pyracylene patches located at the midsection of the fullerene cage. Thus, the Sc_3N moiety is strongly bonded to the cage preventing any free rotation. This is in contrast to their theoretical calculation of $Sc_3N@C_{80}$ (as discussed in Section 6.2) where the Sc_3N shows a free rotation within the C_{80} cage.

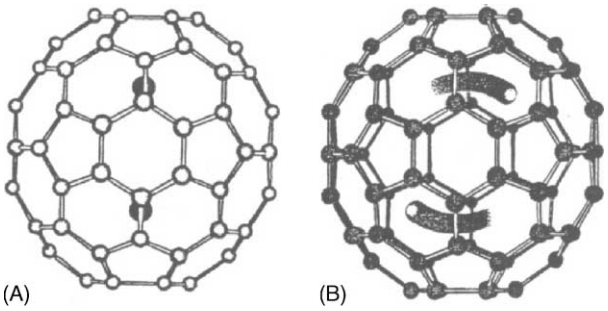

Fig. 14. (A) Optimized D_{2h} structure of $La_2@C_{80}$. (B) Circular motion of the two La atoms inside the I_h cage of C_{80}. Reproduced from Ref. [88] with permission.

6. C_{80}

The C_{80} cage consists of twelve pentagons and thirty hexagons. There are seven IPR-satisfying structures (D_2, D_{5d}, C_{2v}(a), C_{2v}(b), D_3, D_{5h} and I_h) for the C_{80} cage [84,85]. The I_h isomer is most unstable; however, it becomes stable upon charge transfer. In this symmetry, there are two types of carbon atoms, 20 atoms with C_{3v} site symmetry and 60 atoms with C_5 site symmetry. Encapsulation of the two La atoms inside the I_h symmetry is most favored as discussed in the next section.

6.1. $La_2@C_{80}$

Theoretical studies (using Gaussian/DFT) by Kobayashi et al. [85] show that the empty C_{80} cage is most stable when it takes the D_2 or D_5 structure, and the D_2 structure has been confirmed later by ^{13}C NMR spectrum which exhibits 20 signals [86]. Their calculations also show that the carbon cage of endohedral $La_2@C_{80}$ takes I_h symmetry as a result of charge-transfer from the La atoms to the carbon cage ($(La^{3+})_2(C_{80})^{6-}$) [87]. This I_h structure is stabilized because the four-fold degenerate HOMO occupied by two electrons can accommodate six more electrons to form the closed shell structure with a large HOMO–LUMO gap. There are no distinct minima in the electrostatic potential indicating that the encapsulated metals can freely rotate inside the C_{80} cage. Furthermore, these workers proposed the overall D_{2h} structure shown in Fig. 14A in which the two La atoms (ca. 3.66 Å apart) are located on a C_2 axis passing through the centers of two hexagons and each La atom is ca. 2.6 Å from the hexagonal carbon atom.

Akasaka et al. [88] carried out ^{13}C as well as ^{139}La NMR studies of $La_2@C_{80}$ to confirm their theoretical predictions. The ^{139}La NMR spectrum measured at 296 K exhibits a single signal at −402.6 ppm with a line width of 113 Hz, suggesting that the two La atoms are equivalent inside the cage. As discussed later, two signals are expected for the C_{80} cage of I_h symmetry. However, the ^{13}C NMR spectrum of ^{13}C-enriched sample (25% ^{13}C) of $La_2@C_{80}$ at 300 K exhibits only one signal at 141.61 ppm (line width, 0.08 ppm) with satellite bands due to the ^{13}C–^{13}C coupling. This was attributed to a near-spherical cage resulting from circular motion of two La atoms inside the carbon cage as illustrated in Fig. 14B. The observed small line width suggests that the two signals expected for I_h symmetry are too close to be observed as separate signals. Since there is a small barrier for such a motion, it should be possible to stop the La atoms at the most stable positions by lowering the temperature. In fact, they observed a broad ^{13}C NMR signal at 258 K which was attributed to an overlap of the 13 signals expected for D_{2h} symmetry. They also observed a single ^{139}La NMR signal at 258 K which is broadened by raising the temperature from 305 to 363 K.

Fig. 15 shows the IR spectrum of $La_2@C_{80}$ in the range from 353 to 83 K obtained by Moriyama et al. [89]. Under I_h symmetry, the 234 ($3 \times 80 - 6$) normal vibrations of its C_{80}^{6-} cage are grouped into the following symmetry species: $3A_g + A_u + 4F_{1g} + 6F_{1u} + 5F_{2g} + 7F_{2u} + 8G_g + 8G_u + 11H_g + 9H_u$. However, only 14 ($3A_g + 11H_g$) are Raman-active, and only 6 ($6F_{1u}$) are IR-active. Their IR spectrum shows one strong band at 1384 cm^{-1} and four weak bands at 1463, 1232, 680 and 505 cm^{-1} which are evident at 83 K. This spectral pattern is in fairly good agreement with the results of their theoretical calculations on the C_{80}^{6-} cage of I_h symmetry. The line width of the 1384 cm^{-1} band decreases

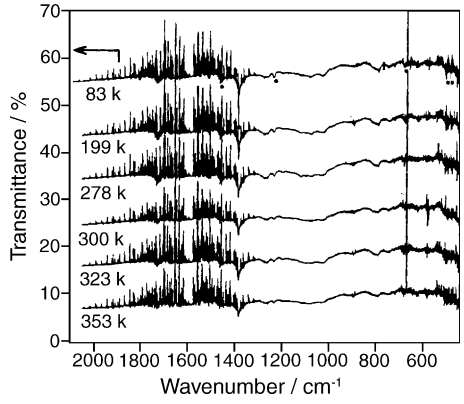

Fig. 15. Infrared spectra of $La_2@C_{80}$ in KBr pellet at temperatures between 83 and 353 K. Reproduced from Ref. [89] with permission.

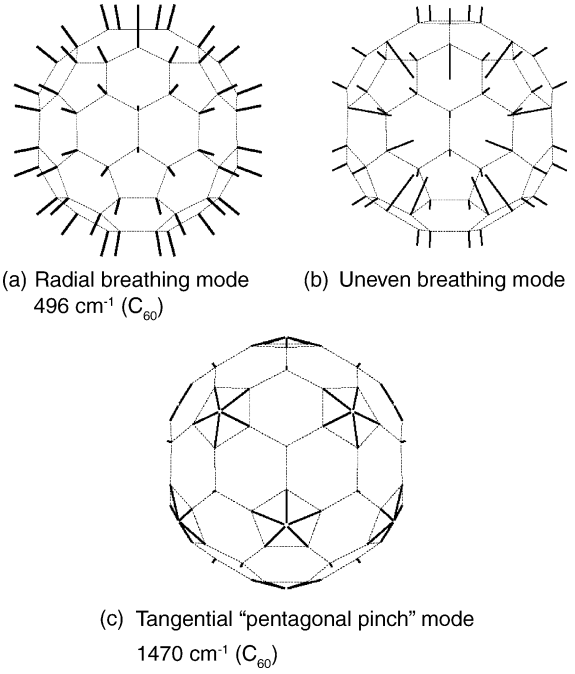

Fig. 16. Mode displacement pattern of the three nondegenerate modes in I_h C_{80}^{6-}: (a) breathing mode $A_g(\nu_1)$, (b) out-of-phase radial mode $A_g(\nu_2)$ and (c) pentagonal-pinch mode $A_g(\nu_3)$. The experimental values of the nondegenerate frequencies of C_{60} are shown.

monotonically upon lowering the temperature from 353 K (14 cm^{-1}) to 83 K (1.5 cm^{-1}). However, the number of observed bands does not reflect the effect of lowering the symmetry from I_h to D_{2h} at low temperatures. According to theoretical calculations on $La_2@C_{80}$ of D_{2h} symmetry, the La–La vibrations in the two directions perpendicular to the La–La axis are at 72 and 66 cm^{-1}. It was not possible, however, to observe these low-frequency modes at low temperature.

Distinction of I_h and D_{2h} symmetries of the C_{80} cage may be made more easily if one measures the polarized Raman spectra of $La_2@C_{80}$. This is because the number of totally symmetric (A_g) vibrations should be only three for the I_h structure while that of the D_{2h} structure is much larger. Thus, the number of polarized bands should increase markedly as the temperature is lowered ($I_h \rightarrow D_{2h}$). Fig. 16 shows schematic of the normal mode displacement pattern of the three totally symmetric vibrations of the C_{80} cage of I_h symmetry [90]. The calculations were performed for a charged C_{80}^{6-} molecule (without any metal cluster in the cage) using first-principles quantum molecular dynamics method in the LDA approach [39]. The corresponding frequencies observed for the I_h–C_{60} are also listed. The radial breathing and pentagonal pinching modes are essentially similar for both cages. However, the "uneven breathing mode" is unusual and unique to the C_{80} cage. It is a totally symmetric mode in which the 60 pentagon atoms move out of phase from the remaining 20 atoms.

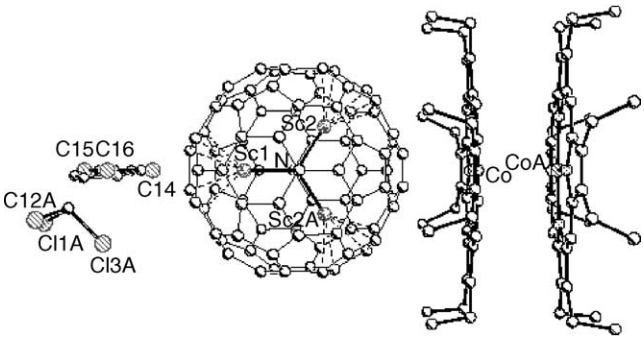

Fig. 17. Crystal structure of $[Sc_3N@C_{80}]Co^{II}(OEP)1.5CHCl_3 0.5C_6H_6$ perpendicular to the mirror plane that bisects Co, Sc1, and N. Reproduced from Ref. [91] with permission.

6.2. $Sc_3N@C_{80}$

Stevenson et al. [91] first prepared a new family of stable endohedral metallofullerenes, $A_{3-n}B_nN@C_{80}$ (n = 0–3, A, B = rare-earth metal) that are stabilized by donation of up to six electrons to the C_{80} cage. The introduction of N_2 during the growth process results in the isolation of a few milligrams of the sample. Members of this class are formed by a trimetallic nitride template (TNT) process, which ensures endohedral formation in the electric-arc process. $Sc_3N@C_{80}$ belongs to this family, where the charge redistribution results in $(Sc_3N)^{6+}(C_{80})^{6-}$. These workers isolated 2–4 mg of $Sc_3N@C_{80}$ from ~60 mg of the product, determined the crystal structure, and measured the UV–vis and ^{13}C NMR spectra of $Sc_3N@C_{80}$. The results confirmed that the Sc_3N moiety is encapsulated in the C_{80} cage of I_h symmetry which is stabilized by the charge-transfer between them. These endohedral fullerenes are the first examples containing relatively large molecules inside the carbon cage. Since the trimetallic nitrides such as Sc_3N and $ErSc_2N$ are stable only in the endohedral state, the preparative method developed by Stevenson et al. has opened a new field of synthetic inorganic chemistry.

Fig. 17 shows the crystal structure of $[Sc_3N@C_{80}]Co^{II}(OEP)\ 1.5CHCl_3 0.5C_6H_6$. It is seen that the trigonal planar Sc_3N moiety is encapsulated inside the C_{80} cage and is close to $Co^{II}(OEP)$ which makes face-to-face contact with another $Co^{II}(OEP)$. The Sc–N distances (2.011 and 1.966 Å) are slightly shorter than the Sc–N bonds in $[(HSiMe_2)_2N]_3Sc(THF)$(average distance, 2.069 Å). In the solid state, the Sc atoms face three pentagons inside the C_{80} cage. Later, X-ray analysis was carried out on a mixed metal analog $ErSc_2N@C_{80}$ [92].

The UV–vis spectrum of $Sc_3N@C_{80}$ shows prominent peaks at 900 and 1140 nm and strong absorption below 1000 nm. The band-gap energy corresponds to the absorption onset (~1560 nm) [91]. It is only 0.8 eV, which is much smaller than that of the 1.3 eV band-gap in $La_2@C_{80}$.

The C_{80} cage of I_h symmetry consists of two types of carbon atoms; 60 atoms are located at the vertices where two hexagons and one pentagon meet (corannulene-type), and the remaining 20 atoms are located at the vertices where three

hexagons meet (pyrene-type). Thus, the ^{13}C NMR spectrum of $Sc_3N@C_{80}$ exhibits two signals at 144.57(corranulene-type) and 137.24 ppm (pyrene-type) in 3:1 intensity ratio. This result suggests that dynamic motion of the Sc_3N moiety inside the cage yields a time-averaged electronic environment of I_h symmetry, and that the Sc_3N cluster is not located at any specific bonding site at least on the NMR time scale at 295 K [91]. Further support of this dynamic behavior is given by the observation that $Sc_3N@C_{80}$ exhibits a single signal in ^{45}Sc NMR spectrum. It is interesting to note that the ^{13}C NMR spectrum of $La_2@C_{80}$ exhibits only one signal in spite of the I_h symmetry of its C_{80} cage due to the reason discussed previously [89].

Krause et al. [93] investigated the IR and Raman spectra of $Sc_3N@C_{80}$ to determine the nature of the C_{80}–Sc_3N interaction. As mentioned earlier, the C_{80} cage of I_h symmetry exhibits 6 IR and 14 Raman fundamentals. The trigonal-planar Sc_3N moiety of D_{3h} symmetry exhibits three IR and three Raman fundamentals. If there is no interaction between them, one should expect 9 IR and 17 Raman fundamentals. However, these workers observed 69 bands (10 IR, 32 Raman and 27 IR/Raman) excluding very weak bands. Violation of the mutual exclusion rule indicates that the I_h symmetry is lowered significantly as a result of the Sc_3N–C_{80} interaction. Fig. 18 shows the IR and Raman spectra obtained at 300 K. It is seen that the Raman spectra obtained by 647 and 514 nm excitations are resonance-enhanced because these lines are close to the electronic transitions at 2.0 and 2.5 eV, respectively.

The vibrations due to the Sc_3N moiety (D_{3h} symmetry) were identified by comparing the IR and Raman spectra of $Sc_3N@C_{80}$ and $Y_3N@C_{80}$. In the 800–200 cm^{-1} region, only three Raman bands at 599, 411 and 210 cm^{-1} are metal-sensitive, and shifted to 709, 429 and 194 cm^{-1}, respectively, by Sc/Y substitution (Fig. 19). These bands were assigned to the antisymmetric stretching (E′, IR/R), symmetric stretching (A_1', R) and in-plane bending (E′, IR/R) vibrations of the planar Sc_3N moiety, respectively. This result is somewhat unexpected since the atomic weight of Y (88.91) is about

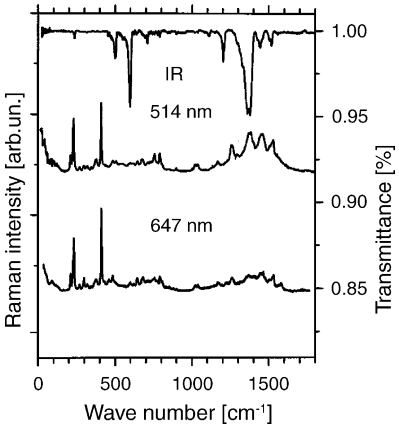

Fig. 18. Infrared and Raman spectrum of $Sc_3N@C_{80}$ at 300 K. Adapted from Ref. [93].

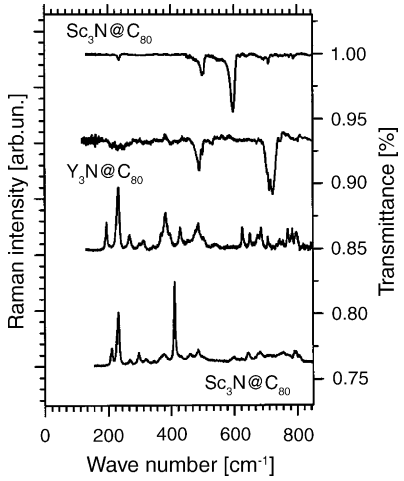

Fig. 19. Low energy infrared and Raman spectrum of $Sc_3N@C_{80}$ and $Y_3N@C_{80}$ at 300 K. Adapted from Ref. [93].

two times larger than that of Sc (44.96). It was attributed to the particular bonding properties of the encaged Y_3N moiety although the origin of this unusual observation is not clear.

Theoretical calculations of $Sc_3N@C_{80}$ by various groups predict different structures. Recently Campanera et al. [83] used DFT to examine the bonding between Sc atoms and the fullerene cage in $Sc_3N@C_{80}$. Their calculations were carried out with the ADF set of programs [28]. They used the local spin density approximation together within the LDA approach [20]. TZ + polarization Slater basis sets (see Section 2.2) were employed to describe the valence electrons of C and N. For $Sc_3N@C_{80}$, the energy difference between isomers of different Sc_3N orientations in the carbon cage is rather small (less than 2 kcal/mol). They find that the C_s symmetry where the three metal ions are oriented toward [6:5] ring junctions has the lowest energy, as shown in Fig. 20. The relative energies for the various isomers result in their conclusion that the Sc_3N unit may easily rotate inside the fullerene cage. This is in contrast to $Sc_3N@C_{78}$ where the Sc ions are strongly linked to the [6:6] ring junctions of pyracylene patches; this bonding restricts the Sc_3N unit to freely rotate within the fullerene cage (vide supra) [83].

Kobayashi et al. [94] have used nonlocal density functional calculations at the BLYP level (a gradient-corrected functional) to calculate the electronic structure of $Sc_{3-n}La_nN@C_{80}$ ($n = 0$–3). For $n = 0$, they find that the large positive charges on Sc are very effective for electrostatic interactions with the negatively charged N atom and the carbon cage. For the pyramidal Sc_3N cluster, however, severe electrostatic repulsion is expected from the carbon cage. Because of this the Sc_3N adopts a planar structure with long Sc–Sc distances in $Sc_3N@C_{80}$. They find that there are two structures of $Sc_3N@C_{80}$ with C_s symmetry that are almost isoenergetic. These results suggest that the Sc_3N ion is not stabilized at specific internal bonding sites but can rotate freely inside the

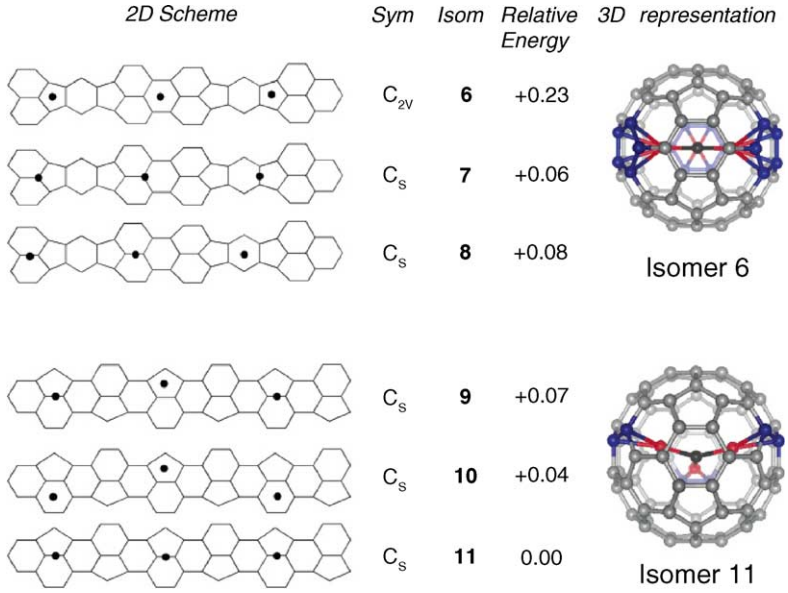

Fig. 20. Relative energies (in eV), symmetries, and carbon chains with schematic position of Sc atoms in a 2D representation for the optimized isomers of $Sc_3N@C_{80}$. The 3D representation for isomers 6 (C_{2v}) and 11 (Cs) shows the connections between the metal ions and carbons. Reproduced from Ref. [83] with permission.

fullerene cage, thus stabilizing the I_h symmetry of the C_{80} cage.

In contrast to the above two theoretical results, calculations by Krause et al. [93] show evidence of a chemical bond between the Sc_3N ion and the C_{80} cage which hinders the rotation of the Sc_3N cluster inside the fullerene cage. They used the DFT scheme employing a nonorthogonal tight-binding model [95] to determine the energy and forces for a given atomic configuration. It turns out that their method is highly transferable and has been applied to determine the structures, total energies, and vibrational properties of carbon molecules, solids and clusters. Their optimized structure is that of C_3 symmetry since the Sc atom is not located exactly below the center of the pentagon and each Sc–C distance is slightly different (±0.2 Å). Their DFT calculations also predict vibrational frequencies and IR intensities of $Sc_3N@C_{80}$ which are in fairly good agreement with those observed. In addition to the internal vibrations of the C_{80} cage and the Sc_3N moiety, four vibrations were predicted under C_3 symmetry in the region below 150 cm^{-1}. These are the vibrations due to the translational and rotational motions of the Sc_3N moiety in the C_{80} cage which are regarded as the Sc_3N–C_{80} vibrations. They were observed around 133, 108, 78 and 48 cm^{-1} for $Sc_3N@C_{80}$ and around 110, 96, 66 and 36 cm^{-1} for $Y_3@C_{80}$. Although this result seems to contradict the ^{13}C NMR study which suggests I_h symmetry, Krause et al. [93] suggest that the isomerization between 20 equivalent configurations can be time-averaged to produce I_h symmetry on the NMR time scale. In contrast to Stevenson et al. [91], these workers [93] noted that a large band gap (slightly over 2.0 eV) resulting from the charge-transfer leads to a close-shell structure which is responsible for its high stability.

The structure of $Sc_3N@C_{80}$ still remains somewhat of an open question since various theoretical works predict different optimized structures. This makes it vital for additional experimental evidence using Raman scattering and IR absorption. Since I_h C_{80} has three Raman-active frequencies of A_g symmetry, polarized Raman studies mentioned earlier should reveal the actual structure of the endohedral fullerene on the vibrational time scale.

Other TNT endohedral fullerenes include $La_3N@C_{80}$. According to Kobayashi et al. [94] the La_3N cluster maintains a pyramidal structure and donates up to eight electrons to the fullerene cage, forming $(La_3N)^{8+}@C_{80}{}^{8-}$. The additional electrons occupy the four-fold degenerate LUMO of C_{80}, resulting in an open shell electronic structure that has a high reactivity. Repulsion between the La atoms and the long La–N bond lengths prevents planarization of the La_3N molecule inside the cage. This makes $La_3N@C_{80}$ less stable than $Sc_3N@C_{80}$.

7. C_{82}

There are nine IPR-satisfying isomeric structures having C_2(a), C_2(b), C_2(c), C_{2v}, C_s(a), C_s(b), C_s(c), C_{3v}(a) and C_{3v}(b) symmetries are for the C_{82} cage [96]. Lebedkin et al. [97] studied the Raman, far-IR and inelastic neutron scattering (INS) spectra of $M@C_{82}$ where M is La, Y, Ce and Gd. Theoretical calculations show that $La@C_{82}$ and $Sc@C_{82}$ have C_{2v} symmetry [98]. In the latter metallofullerene, Sc ($3d^14s^2$) atom prefers to donate two valence electrons to the C_{82} cage because of the low lying 'd' orbitals, whereas La donates all three valence electrons to the fullerene cage. In $Gd@C_{82}$, three valence electrons of Gd are transferred to the

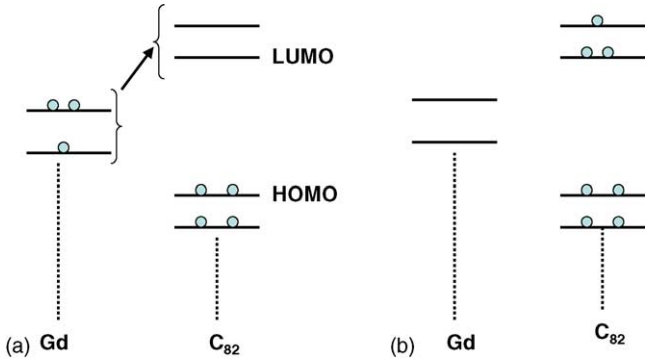

Fig. 21. Electron transfer between Gd and C_{82} in Gd@C_{82}. Adapted from Ref. [6].

LUMO level of C_{82}. Each of the occupied orbitals of C_{82} has a very small tail on the 5d of Gd as a result of a slight back transfer. However, the UV–vis spectra reflect only the orbital picture shown in Fig. 21.

Fig. 22 shows the Raman spectra of monometallic endohedral fullerenes obtained by Lebedkin et al. [97] The spectra above 200 cm^{-1} are very similar indicating a similar carbon cage structure for all four compounds. One of the three structures having C_2 symmetry is most probable according to ^{13}C NMR and theoretical studies by other workers. In contrast, the metal-sensitive bands are observed below 200 cm^{-1}; at 183, 163, 162 and 155 cm^{-1} respectively, for the Y, La, Ce and Gd compounds. If the metal–cage vibration is approximated by a diatomic vibrator, its frequency, ν (cm^{-1}), is given by

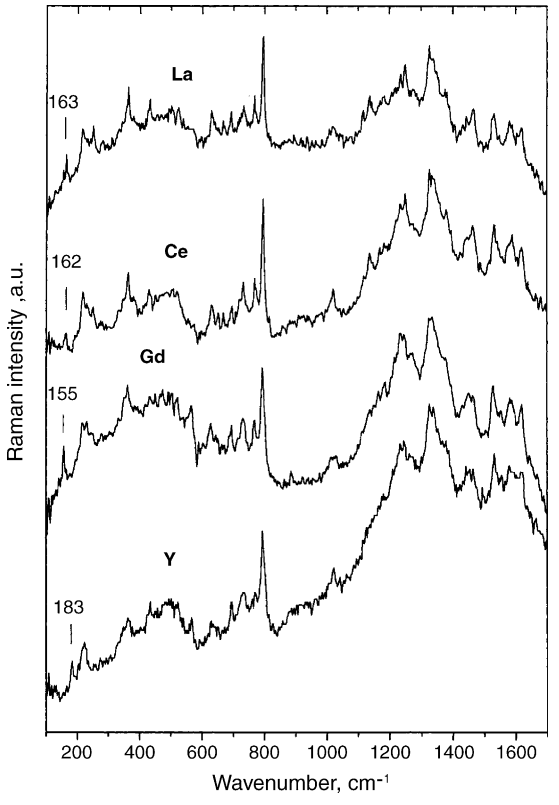

Fig. 22. Raman spectra of M@C_{82} metallofullerenes, M = La, Y, Ce, Gd. Adapted from Ref. [97].

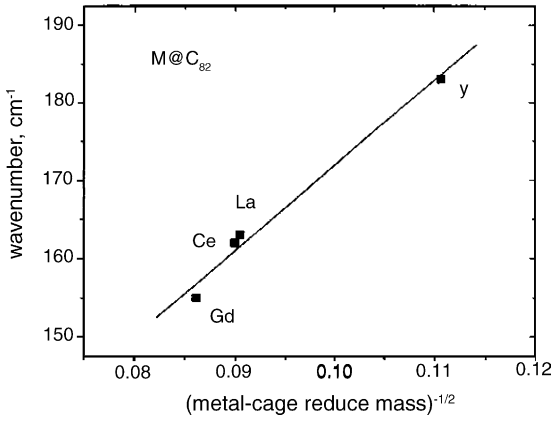

Fig. 23. Dependence of the Raman frequency of the metal-to-cage vibration in M@C_{82} on the reduced mass of the endohedral metal atom. Adapted from Ref. [97].

$$\nu = 4.12\left(\frac{f}{\mu}\right)^{1/2}, \tag{10}$$

where f is the force constant (dyne/cm) and μ is the reduced mass (atomic weight unit) of the M–C_{82} molecule. Fig. 23 [97] shows a linear plot obtained between ν and $\mu^{-1/2}$ from which the average value of f was calculated to be 1.75×10^5 dyne/cm. These results indicate that the magnitude of the M–C_{82} interaction is similar among the four compounds and the M–C_{82} bonding is essentially ionic, namely, M^{3+}–$C_{82}{}^{3-}$.

The IR spectra above 200 cm^{-1} are also similar for the four compounds. However, the Y and La compounds exhibit very strong and broad bands near 54 and 50–45 cm^{-1}, respectively. In contrast to the "longitudinal" metal–cage vibrations observed in the Raman spectra, these low-frequency IR bands were attributed to the "lateral" metal–cage vibrations.

Krause et al. [99,100] measured the Raman and IR spectra of Tm@C_{82} and Gd@C_{82}. The Raman spectra of the three isomers of Tm@C_{82} are clearly different in the high-frequency region but their metal–cage vibrations appear in the same region (117 cm^{-1} for isomers A and B and 116 cm^{-1} for isomer C). These values are significantly lower than that expected from a linear plot obtained for a series of M^{3+}–$C_{82}{}^{3-}$ type compounds. Thus, the Tm^{2+}–$C_{82}{}^{2-}$ formulation was suggested to indicate a weaker ionic interaction.

Xu et al. [101] isolated four isomers (I, II, III and IV) of Ca@C_{82} and obtained the UV–vis–NIR spectra shown in Fig. 24(a). Isomers II and III exhibit distinct absorption onsets at around 1000 and 1200 nm, respectively, whereas isomers I and IV show less distinct onsets at around 1800 nm. In general, these spectra exhibit much more distinctive structures than those containing group IIIA metals such as Sc, Y (Fig. 24(c)) and La. As stated earlier, the electronic state of M@C_{82} (M = Y and La) is expressed as $M^{3+}C_{82}{}^{3-}$.

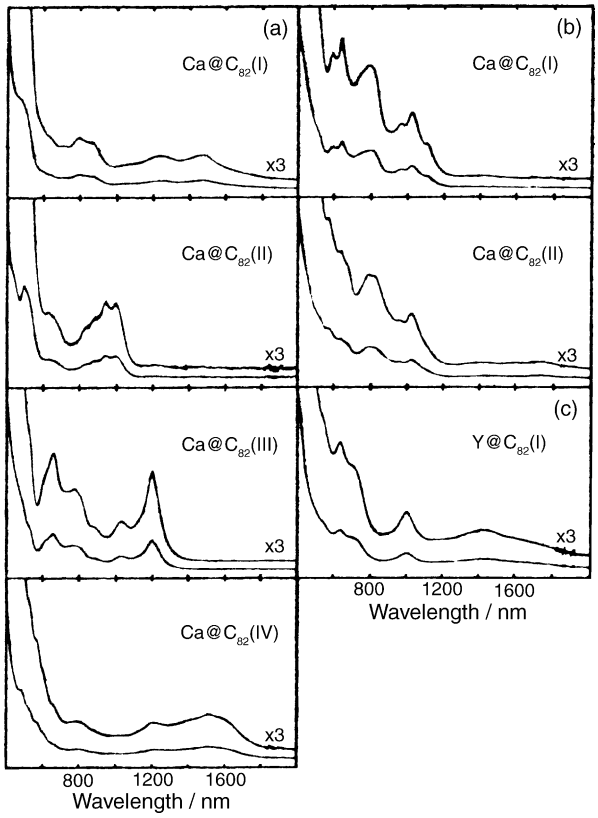

Fig. 24. UV–vis–NIR absorption spectra of (a) Ca@C_{82}(I–IV), (b) Ca@C_{82}(I, II), and (c) Y@C_{82}(I) for comparison. Reproduced from Ref. [101] with permission.

Thus, the $M^{2+}C_{82}{}^{2-}$ formulation was suggested for Ca@C_{82}.

The exact position of the metal in the C_{82} cage cannot be determined by spectroscopic methods. Using synchrotron powder diffraction method, Nishibori et al. [102] were able to determine the cage symmetry of Sc@C_{82} (isomer I) to be C_{2v} and locate the Sc atom at an off-center position on the C_2 axis as shown in Fig. 25. The nearest Sc–C distance obtained from the charge density map was 2.53(8) Å and the Sc–C_{82} charge-transfer was estimated to be 2.2 e. This work was extended to Sc_3@C_{82} which contains an equilateral triangular Sc cluster

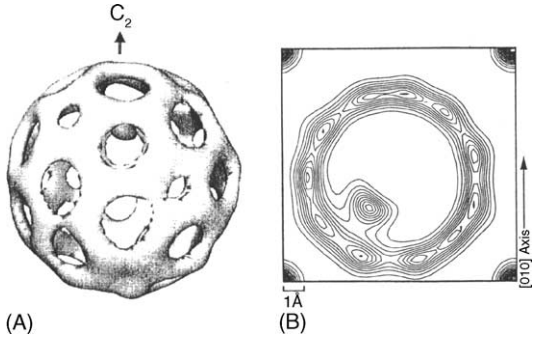

Fig. 25. (A) C_{2v} cage symmetry of Sc@C_{82} where the Sc atom is located at an off-center position on the C_2 axis. (B) Electron density distribution of Sc@C_{82} for the (1 0 0) section. Reproduced from Ref. [102] with permission.

[103]. It was found that the overall symmetry is C_{3v} and the Sc–Sc distance is 2.3(3) Å. In this case, the charge-transfer state is expressed as $Sc_3{}^{3+}$@$C_{82}{}^{3-}$.

Akasaka et al. [104] prepared the La@$C_{82}{}^-$ anion which exhibits a unique stability toward air and water and determined its symmetry by ^{13}C NMR spectroscopy. A-form exhibits 24 lines which are expected for C_{2v} symmetry while B-form shows 38 lines confirming its C_s symmetry.

Recently Inoue et al. [105] isolated an endohedral fullerene, Y_2@C_{84}, which was found to be a metal carbide (Y_2C_2) encapsulated in the C_{82} cage, namely, (Y_2C_2)@C_{82}. The electronic spectrum exhibits two bands at 684 and 880 nm with the onset of the absorption at 1100 nm. From the analysis of the 17 line ^{13}C NMR spectrum, it was suggested that the Y_2C_2 moiety takes a diamond-shaped structure and rotates rapidly inside the spherical C_{82}–C_{3v} cage. Similar results are reported previously for (Sc_2C_2)@C_{84} discussed in the following section.

8. C_{84}

The C_{84} cage can take 24 isomeric structures as shown by Manolopoulos and Fowler [84]. Inakuma et al. [106] isolated the three isomers (I, II and III) of Sc_2@C_{84} and determined their structures by ^{13}C NMR spectroscopy. As shown in Fig. 26, isomer I exhibits 38 lines of nearly equal intensity and eight additional lines of half intensity marked by asterisks. Isomer II exhibits 18 lines plus 6 lines of half intensity,

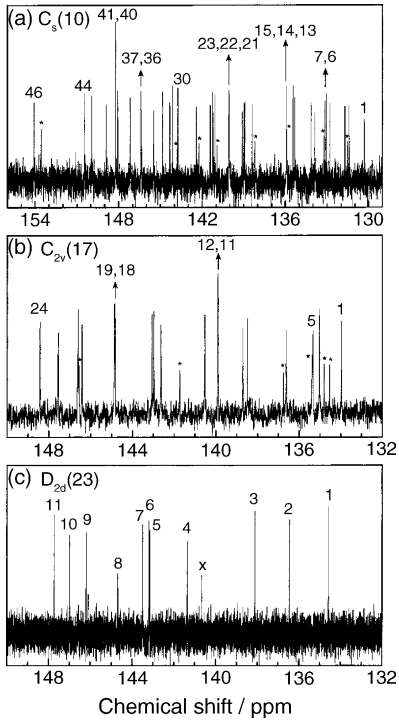

Fig. 26. ^{13}C NMR spectra of Sc_2@C_{84}(I, II, III) in CS_2 at room temperature. Reproduced from Ref. [106] with permission.

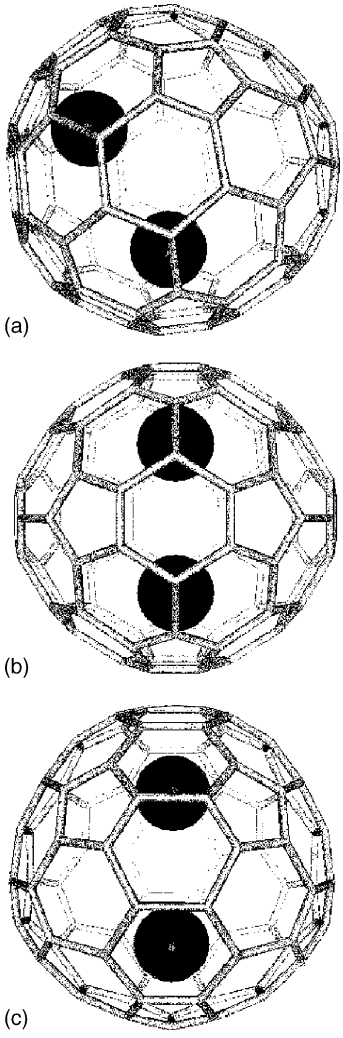

Fig. 27. Molecular structures for $Sc_2@C_{84}$(I, II, III). Reproduced from Ref. [106] with permission.

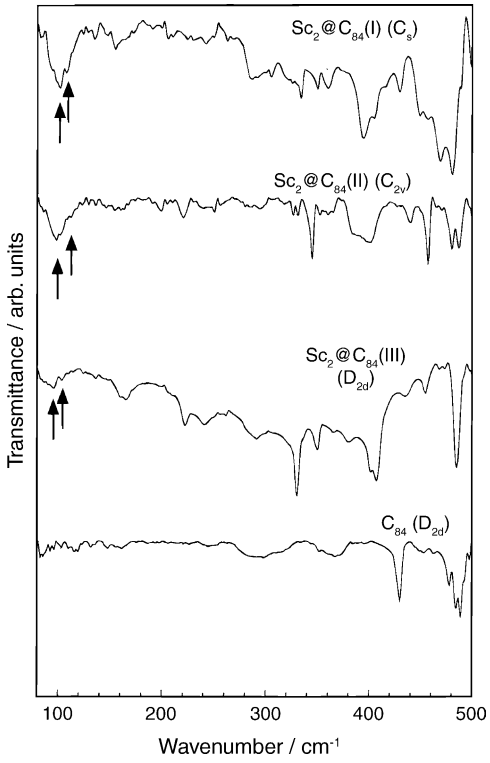

Fig. 28. Far-IR spectra of $Sc_2@C_{84}$(I, II, III) and C_{84} at room temperature. The metal–cage modes are indicated by arrows. Reproduced from Ref. [106] with permission.

and isomer III exhibits 10 lines plus one line of half intensity. Based on these observations, the symmetries of isomers I, II and III are definitively assigned to C_S, C_{2v} and D_{2d}, respectively. The molecular structures consistent with these NMR data are shown in Fig. 27 [106]. The D_{2d} structure of isomer III has been confirmed by synchrotron X-ray diffraction studies [107] and topological analysis of electron density distribution [108].

The UV–vis–NIR spectra of the three isomers are clearly different from each other. Isomer I shows absorption maxima (or shoulders) at 1204, 1045, 862, 730 and 660 nm, whereas isomer II exhibits broad absorptions at around 1770, 1425 and 1000 nm. In contrast, isomer III shows no absorption in the 1300–2000 nm region. The red-shift of the absorption onset of isomer II relative to I and III accounts for the much lower production efficiency and stability of isomer II relative to isomers I and III.

The far-IR spectra of the three isomers of $Sc_2@C_{84}$ and the empty C_{84} cage (D_{2d} symmetry) are compared in Fig. 28 [106]. The metal–cage vibrations appear as the broad bands around 100 cm^{-1} which consist of two bands (marked by arrows) and weak bands near 160–165 cm^{-1}. The corresponding Raman spectra are shown in Fig. 29 [106] where the arrows indicate metal–cage vibrations. These metal–cage vibrations were assigned based on a linear three-mass oscillator model [106] shown in Fig. 30. In the case of isomer III of D_{2d} symmetry [109] the Sc–C_{84} cage modes were assigned at ~250 cm^{-1} (symmetric stretch), ~170 cm^{-1} (antisymmetric stretch), and ~125 cm^{-1} (bending). The calculated Sc–C_{84} stretching force constant was 1.19 dyne/cm which is close to those of Tm@C_{82} (1.18 dyne/cm for isomer A). Since the latter is known to be $Tm^{2+}C_{82}{}^{2-}$, the charge state of the Sc atoms in $Sc_2@C_{84}$ was concluded to be near 2+.

$Sc_2C_2@C_{84}$ is a highly stable compound, and Wang et al. [110] were able to isolate 3.5 mg of the sample to carry out UV–vis, ^{13}C NMR and synchrotron X-ray diffraction studies. The UV–vis spectrum exhibits an absorption onset at 1410 nm and a strong absorption at ca. 600 nm. This is markedly different from those of $Sc_2@C_{84}$(I, II and III) [106]. The ^{13}C NMR spectrum shown in Fig. 31 consists of 11 signals similar to that of $Sc_2@C_{84}$(III) of D_{2d} symmetry plus one extra signal at 91.99 ppm (signal 12). The former 11 signals are due to the carbon atoms of the cage whereas the latter originates in the sp-hybridized carbide carbon atom. The molecular structure determined by synchrotron X-ray powder diffraction studies show that the Sc_2C_2 moiety takes a diamond-shaped structure with the Sc–Sc and C–C dis-

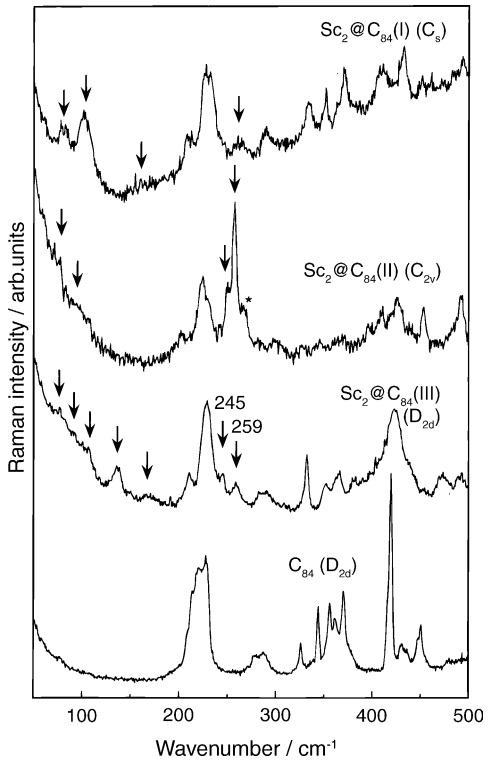

Fig. 29. Raman spectra of $Sc_2@C_{84}$(I, II, III) and C_{84} at room temperature. The metal–cage modes are indicated by arrows. Reproduced from Ref. [106] with permission.

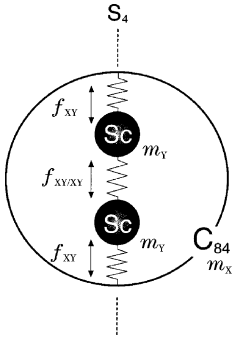

Fig. 30. Three mass oscillator model for the metal–cage vibration of a $Sc_2@C_{84}$(III) molecule. The scandium ions of mass m_Y are bonded to the rigid C_{84} cage of mass by a valence force constant. Reproduced from Ref. [106] with permission.

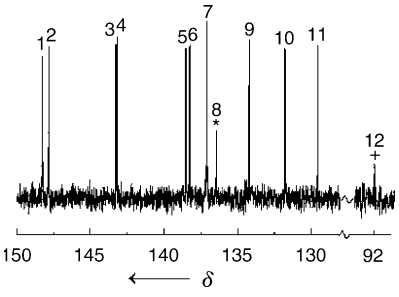

Fig. 31. ^{13}C NMR spectrum of $Sc_2C_2@C_{84}$ in CS_2 solution. Reproduced from Ref. [110] with permission.

tances being 4.29 and 1.42 Å, respectively. The Sc–C distance (2.26 Å) is close to that of ScC_2 (2.135 Å) which was theoretically predicted. The compound is formulated as $(Sc_2C_2)^{2+}@C_{84}{}^{2-}$ since the charge density distribution studies show that the Sc_2C_2 moiety is in the 2+ state.

9. Summary and prospect

This review describes the current status of structural and spectroscopic studies on endohedral fullerenes. These studies have shed light on the structure of the carbon cage, the location and the structure of the encapsulated species inside the cage and the nature of interaction between them. Endohedral fullerenes are highly important not only for their unique structures but also for their potential to become superconducting materials. Thus far, endohedral fullerene research has been hindered by the limited availability of the sample (typically in the mg–μg range). This situation will drastically change once preparative techniques are improved and a variety of species are encapsulated inside the carbon cage. Encapsulation is a novel synthetic method to prepare chemical species which are highly unstable "outside the carbon cage". Many small inorganic species thus far unknown may be prepared by using the current and improved techniques.

Acknowledgements

We would like to thank Dr. Gary Adams of Arizona State University for the pictorial representation of the totally symmetric vibrations in I_h C_{80} and other useful discussions. One of us (SG) thanks José Menéndez and John B. Page for invaluable insights in the field of light scattering from fullerenes. We thank Carsten Ullrich for valuable comments on the theoretical methodologies.

References

[1] H.W. Kroto, J.R. Heath, S.C. O'Brien, R.F. Curl, R.E. Smalley, Nature 318 (1985) 162.
[2] L.S. Wang, C. Conceicao, C. Jin, R.E. Smalley, Chem. Phys. Lett. 182 (1991) 5.
[3] O.V. Boltalina, I.N. Ioffe, I.D. Sorokin, L.N. Sidorov, J. Phys. Chem. 101 (1997) 9561.
[4] J.R. Heflin, D. Marciu, C. Figura, S. Wang, P. Burbank, S. Stevenson, H.C. Dorn, Appl. Phys. Lett. 72 (1998) 2788.
[5] D.S. Bethune, R.D. Johnson, J.R. Salem, M.S. de Vries, C.S. Yannoni, Nature 366 (1993) 123.
[6] T. Akasaka, S. Nagase (Eds.), Endofullerenes: A New Family of Carbon Clusters, Kluwer Academic Publishers, 2002.
[7] S. Nagase, K. Kobayashi, T. Akasaka, Bull. Chem. Soc. Jpn. 69 (1996) 2131.
[8] S. Nagase, K. Kobayashi, T. Akasaka, J. Mol. Struct. (Theochem.) 398 (1997) 221.
[9] M. Krause, H. Kuzmany, in: T. Akasaka, S. Nagase (Eds.), Endofullerenes: A New Family of Carbon Clusters, Kluwer Academic Publishers, 2002, p. 169.

[10] F. Rioux, J. Chem. Ed. 71 (1994) 464.
[11] M.L. Cohen, V.H. Crespi, W.E. Billups, A. Ciufolini (Eds.), Buckminsterfullerenes, VCH Publishers, 1993, p. 197.
[12] J. Cioslowski, Electronic Structure Calculations on Fullerenes and Their Derivatives, Oxford University Press, New York, 1995.
[13] I.N. Levine, Quantum Chemistry, Prentice-Hall, New Jersey, 1991.
[14] M. Born, J.R. Oppenheimer, Ann. Physik 84 (1927) 457.
[15] E.R. Davidson, D. Feller, Chem. Rev. 86 (1986) 681.
[16] Gaussian 03, Gaussian, Inc., Pittsburgh, PA, 2003.
[17] W. Kohn, L.J. Sham, Phys. Rev. 140 (1965) A1133.
[18] A.P. Sutton, Electronic Structure of Materials, Oxford University Press, 1994.
[19] P. Hohenberg, W. Kohn, Phys. Rev. 136 (1964) B864.
[20] S.H. Vosko, L. Wilk, M. Nusair, Can. J. Phys. 58 (1980) 1200.
[21] J.P. Perdew, Y. Wang, Phys. Rev. B 45 (1992) 13244.
[22] D.M. Ceperley, B.J. Adler, Phys. Rev. Lett. 45 (1980) 566.
[23] R.O. Jones, O. Gunnarsson, Rev. Mod. Phys. 61 (1989) 689.
[24] J.P. Perdew, K. Burke, M. Ernzerhof, Phys. Rev. Lett. 77 (1996) 3865.
[25] A.D. Becke, J. Chem. Phys. 98 (1993) 5648.
[26] A.D. Becke, Phys. Rev. A 38 (1988) 3098.
[27] C. Lee, W. Yang, R.G. Parr, Phys. Rev. B 37 (1988) 785.
[28] ADF 2. 3 User's Guide, Chemistry Department, Vrije Universiteit, Amsterdam, The Netherlands, 1997;
G. te Velde, F.M. Bickelhaupt, E.J. Baerends, C. Fonseca Guerra, S.J.A. van Gisbergen, J.G. Snijders, T. Ziegler, J. Comput. Chem. 22 (1991) 931.
[29] T. Koopmans, Physica 1 (1934) 104.
[30] J. Cioslowski, E.D. Fleischmann, J. Chem. Phys. 94 (1991) 3730.
[31] J. Cioslowski, K. Raghavachari, J. Chem. Phys. 98 (1993) 8734.
[32] T. Guo, R.E. Smalley, G.E. Scuseria, J. Chem. Phys. 99 (1993) 352.
[33] M.S. Dresselhaus, G. Dresselhaus, P.C. Eklund, Science of Fullerenes and Carbon Nanotubes, Academic Press, San Diego, 1996.
[34] M.S. Dresselhaus, G. Dresselhaus, P.C. Eklund, J. Raman Spectrosc. 27 (1996) 351.
[35] J. Menéndez, J.B. Page, in: M. Cardona, G. Güntherodt (Eds.), Light Scattering in Solids VIII, Springer Verlag Berlin, 2000, pp. 27–95.
[36] A.A. Quong, M.R. Pederson, J.L. Feldman, Solid State Commun. 87 (1993) 535.
[37] X.Q. Wang, C.Z. Wang, K.M. Ho, Phys. Rev. B 48 (1993) 1884.
[38] P. Giannozzi, S. Baroni, J. Chem. Phys. 100 (1994) 8537.
[39] G.B. Adams, J.B. Page, O.F. Sankey, K. Sinha, J. Menendez, D.R. Huffman, Phys. Rev. B 44 (1991) 4052;
G.B. Adams, J.B. Page, O.F. Sankey, M. O'Keefe, Phys. Rev. B 50 (1994) 17471.
[40] J. Harris, Phys. Rev. B 31 (1985) 1770.
[41] R.A. Jishi, R.M. Mirie, M.S. Dresselhaus, Phys. Rev. B 45 (1992) 13685.
[42] J.L. Feldman, J.Q. Broughton, L.L. Boyer, D.E. Reich, M.D. Kluge, Phys. Rev. B 46 (1992) 1273.
[43] G. Onida, G. Benedek, Europhys. Lett. 18 (1992) 403.
[44] M. Fanti, G. Orlandi, F. Zerbetto, J. Phys. B: Atom. Mol. Opt. Phys. 29 (1996) 5065.
[45] S. Sanguinetti, G. Benedek, M. Righetti, M. Onida, Phys. Rev. B 50 (1994) 6743.
[46] G.W. Chantry, in: A. Anderson (Ed.), The Raman Effect, vol. 1, Dekker, New York, 1971, p. 49.
[47] S. Guha, J. Menéndez, J.B. Page, G.B. Adams, Phys. Rev. B 53 (1996) 13106;
S. Guha, J. Menéndez, J.B. Page, G.B. Adams, Phys. Rev. B 56 (1997) 15431.
[48] J. Fabian, Phys. Rev. B 53 (1996) 13864.
[49] K. Nakamoto, M. McKinney, J. Chem. Ed. 77 (2000) 775.
[50] D.S. Bethune, G. Meijer, W.C. Tang, H.J. Rosen, W.G. Golden, H. Seki, C.A. Brown, M.S. de Vries, Chem. Phys. Lett. 179 (1991) 181.
[51] S. Guha, J. Menéndez, J.B. Page, G.B. Adams, G.S. Spencer, J.P. Lehman, P. Giannozzi, S. Baroni, Phys. Rev. Lett. 72 (1994) 3359.
[52] The line shape of the 1470 cm^{-1} mode mimics the mass spectrum since the isotope effect on this vibration can be described in terms of the first-order nondegenerate perturbation theory.
[53] R.A. Jishi, M.S. Dresselhaus, G. Dresselhaus, K.-A. Wang, P. Zhou, A.M. Rao, P.C. Eklund, Chem. Phys. Lett. 206 (1993) 187.
[54] B. Chase, N. Herron, E. Holler, J. Phys. Chem. 96 (1992) 4262.
[55] J. Ren, J.B. Page, J. Menéndez, J. Raman Spectrosc. 34 (2003) 380.
[56] G.B. Adams, J.B. Page, in: P.C. Eklund, A.M. Rao (Eds.), Fullerene Polymers and Fullerene–Polymer Composites, Springer Verlag, Berlin, 2000, p. 185.
[57] A.F. Hebard, M.J. Rosseinsky, R.C. Haddon, D.W. Murphy, S.H. Glarum, T.T.M. Palstra, A.P. Ramirez, A.R. Kortan, Nature 350 (1991) 600.
[58] R.C. Haddon, Acc. Chem. Res. 25 (1992) 127.
[59] S. Leach, M. Vervloet, A. Desprès, E. Bréheret, J.P. Hare, T.J. Dennis, H.W. Kroto, R. Taylor, D.R.M. Walton, Chem. Phys. 160 (1992) 451.
[60] G. Gensterblum, J.J. Pireaux, P.A. Thiry, R. Caudano, J.P. Vigneron, Ph. Lambin, A.A. Lucas, W. Krätschmer, Phys. Rev. Lett. 67 (1991) 2171.
[61] R. Tycko, J. Phys. Chem. Solids 54 (1993) 1713.
[62] S. Saito, A. Oshiyama, Phys. Rev. Lett. 66 (1991) 2637.
[63] F. Negri, G. Orlandi, F. Zerbetto, J. Am. Chem. Soc. 114 (1992) 2909.
[64] B. Kessler, A. Bringer, S. Cramm, C. Schlebusch, W. Eberhardt, S. Suzuki, Y. Achiba, F. Esch, M. Barnaba, D. Cocco, Phys. Rev. Lett. 79 (1998) 3026.
[65] B. Pietzak, A. Weidinger, K.-P. Dinse, A. Hirsch, in: T. Akasaka, S. Nagase (Eds.), Endofullerenes: A New Family of Carbon Clusters, Kluwer Academic Publishers, 2002.
[66] M. Waiblinger, K. Lips, W. Harneit, A. Weidinger, E. Dietel, A. Hirsch, Phys. Rev. B 63 (2001) 045421.
[67] K. Yamamoto, M. Saunders, A. Khong, R.J. Cross Jr., M. Grayson, M.L. Gross, A.F. Benedetto, R.B. Weisman, J. Am. Chem. Soc. 121 (1999) 1591.
[68] T. Kanbara, Y. Kubozono, Y. Takabayashi, S. Fujiki, S. Iida, Y. Haruyama, S. Kashino, S. Emura, T. Akasaka, Phys. Rev. B 64 (2001) 113403.
[69] H. Jantoljak, N. Krawez, I. Loa, R. Tellgmann, E.E.B. Campbell, A.P. Litvinchuk, C. Thomsen, Z. Phys. Chem. (Munchen) 200 (1997) 157.
[70] T. Ogawa, T. Sugai, H. Shinohara, J. Am. Chem. Soc. 122 (2000) 3538.
[71] T. Inoue, Y. Kubozono, S. Kashino, Y. Takabayashi, K. Fujitaka, M. Hida, M. Inoue, T. Kanbara, S. Emura, T. Uruga, Chem. Phys. Lett. 316 (2000) 381.
[72] J.J. Rehr, R.C. Albers, Rev. Mod. Phys. 72 (2000) 621.
[73] R. Klingeler, G. Kann, I. Wirth, S. Eisebitt, P.S. Bechthold, M. Neeb, W. Eberhardt, J. Chem. Phys. 115 (2001) 7215.
[74] C.-R. Wang, T. Kai, T. Tomiyama, T. Yoshida, Y. Kobayashi, E. Nishibori, M. Takata, M. Sakata, H. Shinohara, Nature 408 (2000) 426.
[75] S. Stevenson, P.W. Fowler, T. Heine, J.C. Duchamp, G. Rice, T. Glass, K. Harich, E. Hajdu, R. Bible, H.C. Dorn, Nature 408 (2000) 427.
[76] L. Dunsch, A. Bartl, P. Georgi, P. Kuran, Synth. Met. 121 (2001) 1113.
[77] T.S.M. Wan, H.-W. Zhang, T. Nakane, Z. Xu, M. Inakuma, H. Shinohara, K. Kobayashi, S. Nagase, J. Am. Chem. Soc. 120 (1998) 6806.
[78] K. Kobayashi, S. Nagase, J. Am. Chem. Soc. 119 (1997) 12693.

[79] S. Nagase, K. Kobayashi, T. Akasaka, J. Mol. Struct. (Theochem.) 462 (1999) 97.
[80] P. Kuran, M. Krause, A. Bartl, L. Dunsch, Chem. Phys. Lett. 292 (1998) 580.
[81] F. Diederich, R.L. Whetten, C. Thilgen, R. Ettl, I. Chao, M.M. Alvarez, Science 254 (1991) 1768;
K. Kikuchi, N. Nakahara, T. Wakabayashi, S. Suzuki, H. Shiromaru, Y. Miyake, K. Saito, I. Ikemoto, M. Kainosho, Y. Achiba, Nature 357 (1992) 142.
[82] M.M. Olmstead, A. de Bettencourt-Dias, J.C. Duchamp, S. Stevenson, D. Marciu, H.C. Dorn, A.L. Balch, Angew. Chem. Int. Ed. 40 (2001) 1223.
[83] J.M. Campanera, C. Bo, M.M. Olmstead, A.L. Balch, J.M. Poblet, J. Phys. Chem. A 106 (2002) 12356.
[84] D.E. Manolopoulos, P.W. Folwer, J. Chem. Phys. 96 (1992) 7603.
[85] K. Kobayashi, S. Nagase, T. Akasaka, Chem. Phys. Lett. 245 (1995) 230.
[86] F.H. Hennrich, R.H. Michel, A. Fischer, S. Richard-Schneider, S. Gilb, M.M. Kappes, D. Fuchs, M. Bürk, K. Kobayashi, S. Nagase, Angew. Chem. Int. Ed. 35 (1996) 1732.
[87] K. Kobayashi, S. Nagase, T. Akasaka, Chem. Phys. Lett. 261 (1996) 502.
[88] T. Akasaka, S. Nagase, K. Kobayashi, M. Wälchli, K. Yamamoto, H. Funasaka, M. Kako, T. Hoshino, T. Erata, Angew. Chem. Int. Ed. 36 (1997) 1643.
[89] M. Moriyama, T. Sato, A. Yabe, K. Yamamoto, K. Kobayashi, S. Nagase, T. Wakahara, T. Akasaka, Chem. Lett. 29 (2000) 524.
[90] S. Guha, G.B. Adams, J.B. Page, W. Graupner, S. Stevenson, H.C. Dorn, A. Erlacher, D. Parlow, K. Nakamoto, Unpublished.
[91] S. Stevenson, G. Rice, T. Glass, K. Harich, F. Cromer, M.R. Jordan, J. Craft, E. Hadju, R. Bible, M.M. Olmstead, K. Maitra, A.J. Fisher, A.L. Balch, H.C. Dorn, Nature 401 (1999) 55.
[92] M.M. Olmstead, A. de Bettencourt-Dias, J.C. Duchamp, S. Stevenson, H.C. Dorn, A.L. Balch, J. Am. Chem. Soc. 122 (2000) 12220.
[93] M. Krause, H. Kuzmany, P. Georgi, L. Dunsch, K. Vietze, G. Seifert, J. Chem. Phys. 115 (2001) 6596.
[94] K. Kobayashi, Y. Sano, S. Nagase, J. Comput. Chem. 22 (2001) 1353.
[95] D. Porezag, Th. Frauenheim, Th. Köhler, G. Seifert, R. Kaschner, Phys. Rev. B 51 (1995) 129471.
[96] S. Nagase, K. Kobayashi, T. Akasaka, J. Comput. Chem. 19 (1998) 232.
[97] S. Lebedkin, B. Renker, R. Heid, H. Schober, H. Rietschel, Appl. Phys. A 66 (1998) 273.
[98] K. Kobayashi, S. Nagase, Chem. Phys. Lett. 282 (1998) 325.
[99] M. Krause, P. Kuran, U. Kirbach, L. Dunsch, Carbon 37 (1999) 113.
[100] M. Krause, M. Hulman, H. Kuzmany, P. Kuran, L. Dunsch, T.J.S. Dennis, M. Inakuma, H. Shinohara, J. Mol. Struct. 521 (2000) 325.
[101] Z. Xu, T. Nakane, H. Shinohara, J. Am. Chem. Soc. 118 (1996) 11309.
[102] E. Nishibori, M. Takata, M. Sakata, M. Inakuma, H. Shinohara, Chem. Phys. Lett. 298 (1998) 79.
[103] M. Takata, E. Nishibori, M. Sakata, M. Inakuma, E. Yamamoto, H. Shinohara, Phys. Rev. Lett. 83 (1999) 2214.
[104] T. Akasaka, T. Wakahara, S. Nagase, K. Kobayashi, M. Waelchli, K. Yamamoto, M. Kondo, S. Shirakura, Y. Maeda, T. Kato, M. Kako, Y. Nakadaira, X. Gao, E. van Caemelbecke, K.M. Kadish, J. Phys. Chem. B 105 (2001) 2971.
[105] T. Inoue, T. Tomiyama, T. Sugai, H. Shinohara, Chem. Phys. Lett. 382 (2003) 226.
[106] M. Inakuma, E. Yamamoto, T. Kai, C.-R. Wang, T. Tomiyama, H. Shinohara, T.J.S. Dennis, M. Hulman, M. Krause, H. Kuzmany, J. Phys. Chem. B 104 (2000) 5072.
[107] M. Takata, E. Nishibori, B. Umeda, M. Sakata, E. Yamamoto, H. Shinohara, Phys. Rev. Lett. 78 (1997) 3330.
[108] K. Kobayashi, S. Nagase, Chem. Phys. Lett. 302 (1999) 312.
[109] M. Krause, M. Hulman, H. Kuzmany, T.J.S. Dennis, M. Inakuma, H. Shinohara, J. Chem. Phys. 111 (1999) 7976.
[110] C.-R. Wang, T. Kai, T. Tomiyama, T. Yoshida, Y. Kobayashi, E. Nishibori, M. Takata, M. Sakata, H. Shinohara, Angew. Chem. Int. Ed. 40 (2001) 397.